

The contribution to the antimatter flux from individual dark matter substructures

Marco Regis^{1,*} and Piero Ullio^{2,†}

¹*Cosmology and Gravity Group, Department of Mathematics and Applied Mathematics,
University of Cape Town, Rondebosch 7701, South Africa*

²*SISSA, Via Beirut 2-4, I-34014 Trieste, Italy and
Istituto Nazionale di Fisica Nucleare, Sezione di Trieste, I-34014 Trieste, Italy*

The local antimatter fluxes induced by an individual dark matter (DM) substructure can be significantly dependent on the proper motion of the source. We derive analytic solutions to the propagation equation for time-dependent positron and antiproton primary sources, finding that the static limit is a fair approximation only for very high energy particles and nearby sources. We discuss weakly interacting massive particle (WIMP) models fitting the PAMELA positron excess and the FERMI all-electron data. We show that, for a single non-static DM point-source, one cannot extract from the data, in a unique way, model independent particle physics observables, such as the WIMP mass, the pair annihilation cross section, and the annihilation yield. The gamma-ray emission associated to WIMP models inducing a significant local flux of positrons or antiprotons is found to be compatible with EGRET measurements, but it can be definitely singled out with the FERMI-LAT telescope.

PACS numbers: 95.35.+d, 95.85.Pw, 95.85.Ry, 98.70.Rz, 98.70.Sa

Keywords: Dark Matter, Indirect Detection, Cosmic-rays

I. INTRODUCTION

The recent measurements of the local cosmic-ray electron and positron fluxes have stimulated a lot of interest in the cosmic-ray field. The sharp rise in the positron fraction detected by PAMELA [1] seems a clear indication of the existence of a nearby positron source in addition to the secondary positron component due to the interaction of primary species with the interstellar medium along propagation. The very recent high-statistic measurement by FERMI [2] of the all-electron flux (namely the flux of electrons plus positrons without charge discrimination), while not confirming previous hints of an anomalous peak by ATIC [3] and PPB-BETS [4], has found a spectral index sensibly harder than the one inferred from past extrapolations for the electron spectrum based on lower energy (and less accurate) data. Such a picture leaves room for a substantial contribution from unconventional (or previously disregarded) lepton sources, and it is very tempting to consider the possibility that a large component of the positron and electron flux is provided by the pair annihilation of dark matter (DM) particles, possibly forming the DM halo of the Milky Way (for early proposals in this direction see, e.g., [5, 6, 7]; for reviews on indirect DM detection see, e.g., [8, 9, 10]). The latest fits of the data with such a component, see, e.g., [11, 12] confirm that this picture is viable. Two general features of the DM-induced source were well-known even from early analyses: i) to match the level of the positron background, the local pair annihilation rate needs to be much larger than the one expected for thermal DM weakly interacting massive particles (WIMPs), within standard assumptions for the Universe thermal history and the local DM distribution; ii) having normalized the annihilation rate to the observed positron flux, there are very stringent bounds on the WIMP model from measurements of the local antiproton flux, disfavouring annihilation modes giving rise to a hadronic yield, and favouring the leptonic channels. DM models fulfilling these requirements have been proposed recently, see, e.g., [13, 14]. For what concerns the first requirement, they mainly focus on a mechanism to account for a mismatch between the thermally averaged annihilation cross section at the freeze-out in the early Universe and a much larger annihilation cross section in the halo today. Alternatively, one could invoke an enhancement in the positron signal based on the presence of a local population of dense dark matter substructures, with the pair annihilation rate being large because the average of the number density of DM pairs is much greater than one half of the square of the mean DM number density (i.e., in terms of the local DM halo density ρ , $\langle \rho^2 \rangle \gg \langle \rho \rangle^2$). When considering an average effect within many realizations of the Milky Way substructure population as extrapolated from current Λ CDM numerical N-body simulations, the mean enhancements in the local cosmic-ray fluxes are typically very modest, possibly below a factor of few [15, 16]. Large effects, at the level needed

*Electronic address: Marco.Regis@uct.ac.za

†Electronic address: ullio@sissa.it

to account for PAMELA and FERMI data, have been claimed instead in connection to a (few) single, very dense, nearby substructure(s) [17, 18, 19, 20]; the price to pay in this case is that one has to refer to a configuration with a very small realization probability according to the N-body simulations, or to rely on a subhalo picture which is less standard.

Both in discussing average effects from a full subhalo population and in tracing the effect of individual substructures, the approach of the recent papers and the vast majority of papers in the literature has been to ignore the fact that one is dealing with a system which is not static, and the emission and propagation of charged particles has been treated in the steady state limit. The distribution of substructures in the Galaxy is not rotationally supported; their typical velocity can be estimated from the total mass density profile of the Milky Way. Assuming for simplicity spherical symmetry for the Galaxy and an isothermal sphere for the subhalo phase-space distribution function, the velocity dispersion for such a distribution is simply equal to $\sqrt{3/2}$ times the value of the circular velocity [21], i.e., assuming 250 km s^{-1} for the local rotational speed [22], about 300 km s^{-1} . An object moving at such speed on an orbit perpendicular to the Galactic plane has a time of crossing of the diffusive halo region for cosmic-rays, say a cylinder with a 4 kpc half-height, of about 10^{15} s . Such value is comparable to the typical confinement time for cosmic rays as estimated in the simplified "leaky-box" propagation models, and to the energy loss timescale for electrons and positrons [23]. This is clearly just a qualitative argument (actually not even referring to the most appropriate quantities, see the discussion below) to illustrate that the effect of proper motion of DM substructure can be relevant. Indeed, we will show that there is the possibility that local antimatter measurements reflect a transient due to DM annihilations in a subhalo, rather than a source to be modeled in the steady state limit.

The paper discusses the main features of the local antimatter fluxes resulting from individual DM substructures, taking proper motion into account. Analytic solutions for the propagation equation, as appropriate for positrons and antiprotons/antideuterons, are presented taking into account the most relevant terms, referring to a simplified description of the diffusion region, the interstellar medium and radiation field (these are the same kind of assumptions which are usually implemented for DM studies in the steady state limit, as well as, most often, to discuss electron/positron fluxes from astrophysical sources). We show results in a few benchmark configurations for the propagation parameters and for the orbit of the DM source. We introduce a few sample possible interpretations for the PAMELA and FERMI positron/electron data, illustrating how sensitive one becomes to different assumptions. In particular, we show that, contrary to the picture extensively discussed in recent analyses, it is no longer true that one can extract from the data, in a unique way, model independent particle physics observables, such as the DM mass, the pair annihilation cross section and the annihilation channel. We also consider the gamma-ray signals associated to this scenario and compare with current limits as well as with the detection prospects in the upcoming future.

The paper is organized as follows. In Section II, we present the description of the particle propagation in the Galaxy. We discuss point-like DM substructures as sources of positrons and compare to PAMELA and FERMI data in Section III and IV, respectively. The contribution to the antiproton flux is presented in Section V. In Section VI, we compute other detectable extra features of the electron/positron flux, such as the associated radiative emission and the dipole anisotropy of the spectrum. Section VII concludes. Details on the solution of the transport equation for positrons and antiprotons are reported in the Appendix.

II. THE COSMIC-RAY PROPAGATION MODEL

The random walk of charged cosmic-rays in the turbulent and regular component of the Galactic magnetic fields is usually treated through an effective description. Defining n the number density per unit total particle momentum of a given particle species (i.e., $n(p)dp$ is the number of particles in the momentum interval $(p, p+dp)$), the propagation equation can be casted in the general form (see, e.g. [24]):

$$\frac{\partial n(\vec{r}, p, t)}{\partial t} = Q(\vec{r}, p, t) + \vec{\nabla} \cdot (D_{xx} \vec{\nabla} n - \vec{v}_c n) + \frac{\partial}{\partial p} p^2 D_{pp} \frac{\partial}{\partial p} \frac{1}{p^2} n - \frac{\partial}{\partial p} \left[\dot{p} n - \frac{p}{3} (\vec{\nabla} \cdot \vec{v}_c) n \right] - \frac{n}{\tau_f} - \frac{n}{\tau_r}. \quad (1)$$

Here Q is the source term, including primary, spallation and decay contributions, D_{xx} is the spatial diffusion coefficient, \vec{v}_c is the convection velocity, diffusive reacceleration is described as diffusion in momentum space and is determined by the coefficient D_{pp} , $\dot{p} \equiv dp/dt$ is the momentum gain or loss rate, τ_f is the time scale for loss by fragmentation, and τ_r is the time scale for radioactive decay. The problem is usually solved for stationary sources and assuming n has reached equilibrium (i.e. setting the left-hand side of the equation to zero), through a fully numerical integration of the general model, see, e.g., the Galprop [25] and the Dragon [26] packages, or implementing (a chain of) semi-analytic solutions valid within a set of simplifying assumptions, see, e.g., [27, 28]. In our analysis we will follow the second route, implementing however solutions of the diffusion equations valid for positron or antiproton primary sources which are non-stationary. As commonly done, we will assume a spatially constant diffusion coefficient and introduce a spatial average for the positron/electron energy loss rate; we will also neglect both convection and reacceleration,

sketching the relative energy dependent effects through an appropriate choice of the momentum scaling of the spatial diffusion coefficient. This very simplified scheme, which is flexible enough to introduce many study cases without neglecting any of the physical effects we wish to discuss, can actually be sufficient for a fair description of some of the key observables in cosmic-ray physics. E.g., Ref. [29] introduces, for the Galprop numerical package, the case of a standard diffusive model with spatial diffusion coefficient of the form:

$$D(p) = \beta D_0 \left(\frac{R}{R_0} \right)^\delta, \quad (2)$$

with β being the particle velocity in unit of the speed of light, R being its rigidity, and with the following parameter choice: $D_0 = 2.5 \cdot 10^{28} \text{ cm}^2 \text{ s}^{-1}$, $R_0 = 4 \text{ GV}$, $\delta = 0.6$ for $R > R_0$ and $\delta = 0$ for $R < R_0$ (having neglected D_{pp} , from now on we will simply label D_{xx} as D). The diffusion region is treated as a cylinder extending from $+h_h$ to $-h_h$ in the vertical direction, with standard primary sources in a thin layer around $z = 0$, and up to R_h in the radial direction; in the example of Ref. [29], $h_h = 4 \text{ kpc}$ and $R_h = 30 \text{ kpc}$. Parameters are tuned to reproduce observational constraints, and in particular the relative abundance of secondary to primary components. Indeed, running the public available version of Galprop within this setup, we find a fairly good fit to the Boron over Carbon ratio data (reduced $\chi^2 = 1.23$ for $R > 4 \text{ GV}$, considering the B/C measurements at high energy by ATIC [30], CREAM [31], HEAO3 [32], and CRN [33], and having assumed a spectral index for primary nuclei of 2.35 and 2.1 for, respectively $R < 40 \text{ GV}$ and $R > 40 \text{ GV}$), and to the antiproton over proton ratio as recently measured by PAMELA. We label this parameter choice as "model A", and take it as reference benchmark case. A comprehensive discussion of the dependence of our results on the propagation model is clearly beyond the scope of this paper; the main trends we will present are essentially insensitive to slight readjustments in the parameter space. One of the most relevant parameters for our discussion is the vertical size of the propagation region h_h . It is well known that the local measurements of secondary to primary ratios are mostly sensitive to D_0/h_h rather than to each of the two parameters. The degeneracy would be broken by local measurements of the so-called "radioactive clocks", namely unstable secondaries, such as ^{10}Be as compared to ^9Be . Such data are however not very accurate at present. We consider two extreme setups: a thin halo model with $h_h = 1 \text{ kpc}$ and a thick model with $h_h = 10 \text{ kpc}$; D_0 is rescaled to, respectively, 0.56 and 4.6 in $10^{28} \text{ cm}^2 \text{ s}^{-1}$ as we find simulating this model with Galprop and refitting the B/C ratio (reduced $\chi^2 = 1.10$ and 1.22; the thin halo model is labeled as "model B", while the thick one as "model C"). Within these models the local primary proton and electron fluxes are reproduced as well (for the electron injection spectrum we take a spectral index of 2.30 at high energy, i.e. above $E = 4 \text{ GeV}$). The spectra obtained with Galprop in our reference cases will be used to as background estimates in the next sections; the local electron and positron flux are computed with the spatially-dependent energy loss terms following from the standard templates for the interstellar radiation field and the magnetic field profile as implemented in the code. When computing primary components from WIMP annihilations we will introduce instead the simplification of a spatially-constant energy loss term, referring to an average value valid in the local neighborhood. In the energy loss configuration "H", which we assume as standard reference, the synchrotron and inverse Compton energy loss terms are driven, respectively, by an average magnetic field in the diffusion region which is about $B = 6 \mu\text{G}$, and a mean background starlight density $U = 0.75 \text{ eV cm}^{-3}$ [34], on top of the cosmic microwave background component. For comparison, we will also consider a template in which both quantities are sharply reduced, assuming $B = 1 \mu\text{G}$ and $U = 0.4 \text{ eV cm}^{-3}$ (we label this energy loss configuration by "L").

III. POSITRONS FROM A DARK MATTER POINT SOURCE

Consider the limit of a point-like dark matter substructure, entering the diffusion region at the point \vec{r}_i at the time t_i and moving along an orbit $\vec{r}_p(t)$ (e.g., $\vec{r}_p(t) = \vec{r}_i + \vec{v}_s(t - t_i)$) if one can approximate such motion as a straight line trajectory with constant velocity \vec{v}_s , with dark matter made of WIMP dark matter particles of mass M_χ , annihilating in pairs with annihilation rate (σv) and positron yield per annihilation dN_{e^+}/dp . The positron dark matter source Q at the position \vec{r} , momentum p and time t , takes the form:

$$Q(\vec{r}, t, p) = \delta^3[\vec{r} - \vec{r}_p(t)] \frac{dN_{e^+}}{dp} \Gamma, \quad (3)$$

where Γ , the total dark matter annihilation rate in the source, contains all terms not depending on spatial coordinates, momentum and time:

$$\Gamma = (\sigma v) \int d\vec{r}_s \frac{\rho_s^2(\vec{r}_s)}{2 M_\chi^2} \equiv (\sigma v) \frac{\rho_0^2}{2 M_\chi^2} \mathcal{V}_s. \quad (4)$$

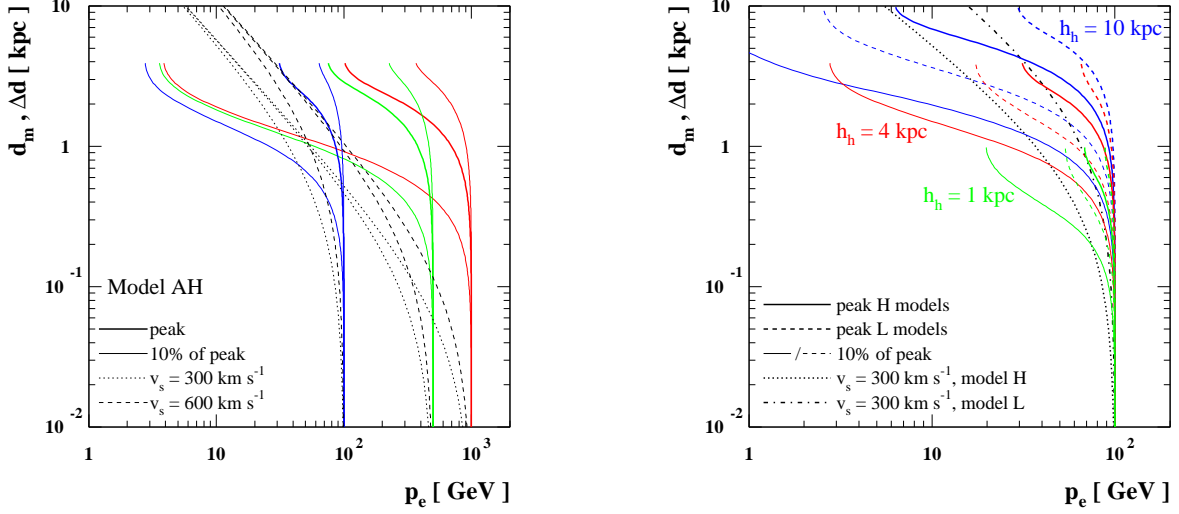


FIG. 1: *Left Panel:* For three sample values of the positron momentum at injection ($p_0 = 100$ GeV, 500 GeV and 1 TeV) and as a function of the positron momentum p_e as measured locally, the proper motion scale Δd (black dashed curves) is compared to distance d_m at which the positron Green function is maximal (thick solid curves) and the range of values for which the Green function is 10% of the maximum (thin solid curves). The propagation model AH is assumed, see the text for more details. *Right Panel:* The same as for the left panel, but for $p_0 = 100$ GeV and the six combinations of diffusion and energy loss models.

Here $\rho_s(\vec{r}_s)$ is the dark matter density profile within the substructure, and the expression after the equivalence sign defines the annihilation volume \mathcal{V}_s , having normalized ρ_s to the reference value $\rho_0 = 0.3$ GeV cm $^{-3}$. The positron number density per unit momentum is given by:

$$n(\vec{r}, p, t) = \frac{\Gamma}{|\dot{p}(p)|} \int_{t_i}^t dt_0 \int_p^{p_{\max}} dp_0 G(\vec{r}, t, p; \vec{r}_p(t_0), t_0, p_0) \frac{dN_{e^+}}{dp_0} \quad (5)$$

The Green function G is given in Appendix A; neglecting boundary conditions it is approximately in the form:

$$G \simeq \frac{1}{\pi^{3/2} [\lambda(p, p_0)]^3} \exp \left\{ - \left[\frac{d(t_0)}{\lambda(p, p_0)} \right]^2 \right\} \delta[(t - t_0) - \Delta\tau(p, p_0)] \quad (6)$$

where we introduced the distance $d = |\vec{r} - \vec{r}_p(t_0)|$ between the source and the observer at the time t_0 , the energy loss timescale $\Delta\tau = \int_p^{p_0} d\tilde{p}/|\dot{p}(\tilde{p})|$, and diffusion length λ , defined through $\lambda^2 = 4 \int_p^{p_0} d\tilde{p} D(\tilde{p})/|\dot{p}(\tilde{p})|$. Looking at this expression, we can guess that including the time dependence in the propagation equation is relevant whenever the variation of d within the time $\Delta\tau$, say $\Delta d \sim v_s \cdot \Delta\tau$, is larger or comparable to λ . Consider the high energy limit, in which the energy loss term scales like $\dot{p}(p) \propto p^2$ and the diffusion coefficient like $D(p) \propto p^\delta$, with $\delta \sim 0.3 - 0.7$; the square of the ratio between Δd and λ goes like:

$$\frac{\Delta d^2}{\lambda^2} \simeq 5 \cdot 10^{-2} \frac{v_{300}^2}{D_1 \dot{p}_1} \frac{1 - \delta}{1 - 0.6} \frac{100^{0.6 - \delta}}{p_{100}^{1 + \delta}} \frac{(1 - \mathcal{R})^2}{1 - \mathcal{R}^{1 - \delta}} \quad (7)$$

where D_1 and \dot{p}_1 are reference values for the diffusion coefficient and energy loss rate at 1 GeV, respectively, 10^{28} cm 2 s $^{-1}$ and -10^{-16} GeV s $^{-1}$, v_{300} the substructure velocity in units of 300 km s $^{-1}$, p_{100} is the positron momentum in the equilibrium distribution in units of 100 GeV, and $\mathcal{R} \equiv p/p_0$ the ratio between such momentum and the momentum of the positron at the source. Being energy losses very effective at high energy, the time spent in the system before losing most of the energy by particles injected with very high momentum tends to be very small. The distance traveled by a DM subhalo in the same timescale is very small as well, and, in this case, proper motion can be safely neglected. An analogous picture occurs when considering cases with small difference between momentum at injection and momentum at equilibrium, and thus with short timescale associated to the electron/positron transport. One sees from Eq. 7 that $\Delta d \ll \lambda$ for $\mathcal{R} \rightarrow 0$ or large p . On the other hand, we expect proper motion to be relevant at intermediate to low energies. This effect is illustrated also in Fig. 1: in the left panel, for a few values of the

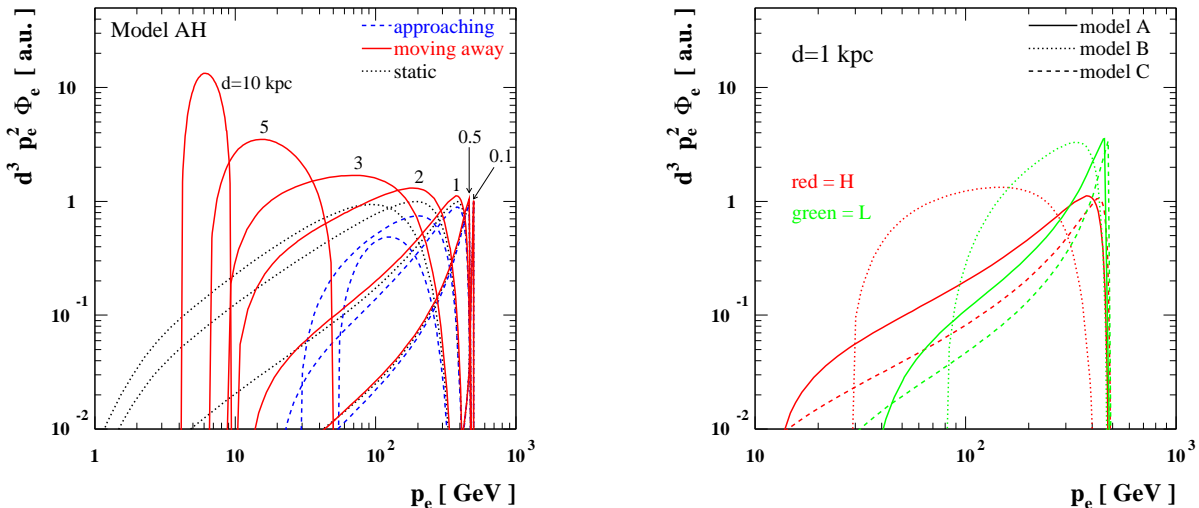


FIG. 2: *Left Panel:* Local positron flux spectral shape for a point-source composed by 500 GeV WIMPs annihilating into monochromatic $e^+ e^-$, and moving along a vertical orbit intersecting the Galactic plane at a short distance from the observer. Each curve refer to a different time of observation, with the distance d of the source from the observer playing the role of time variable. This is useful since we can compare with the spectra one obtains for static sources placed at the same distances. The positron flux is multiplied by $p^2 d^3$ to match the approximate scaling in the static limit. *Right Panel:* For a give time of observation (namely, fixing $d = 1$ kpc), predictions for the flux within our benchmark setups for the propagation model.

momentum at the source p_0 , we compute λ as a function of p and, correspondingly, find the value of d_m , namely, the distance from us along the direction perpendicular to the Galactic plane at which the exact Green function G reaches its maximum (thick solid lines). Neglecting boundary conditions as in Eq. (6), we would simply find $d_m = \sqrt{3/2} \lambda$; in the plot the scaling of d_m with p gets more rapid when the distance approaches the vertical boundary of the diffusion region at $h_h = 4$ kpc (the propagation model "AH" is assumed in the plot). Also displayed are the range of distances within which the Green function is larger than one tenth of its maximum and our estimate for Δd , as defined above. In the right panel, we plot the same quantities for a single injected momentum ($p_0 = 100$ GeV), but looping over the three propagation models and the two energy loss configurations as specified in the previous Section. In both panels, comparing d_m and the 10% range to Δd , one sees that there are large p intervals over which proper motion effects are expected to be large.

To discuss the contribution to the local positron flux Φ_e from a single point source, we start considering the sample case of a source moving with constant velocity $v_s = 300$ km s $^{-1}$, on a trajectory which is perpendicular to the Galactic plane, intersecting the plane at a small distance from the Sun (say 10 pc, the precise value has little relevance for the discussion). To emphasizes propagation effects, we refer to a dark matter model, of given mass and total annihilation rate, with prompt annihilation into $e^+ e^-$ pairs, i.e. with a monochromatic positron spectrum $dN_{e^+}/dp \simeq \delta(p - M_\chi)$. In Fig. 2 we fix $M_\chi = 500$ GeV and show the shape of the induced local positron fluxes in a few sample cases. In the left panel, each curve refers to a different time of observation, but rather than labeling them by time steps, we indicate the distance d of the source from the observer, along the trajectory and at the time when the positron flux is measured (dashed lines for an approaching source, solid line for a source which has passed nearby and now is moving away; for reference, in the example we are considering, a shift of 1 kpc in d corresponds to a time interval $\Delta t \simeq 10^{14}$ s, i.e. about an order of magnitude lower than the typical "escape time" for particles of these energies as extrapolated in simple "leaky box" propagation models). For comparison, we also show the case of static sources (dotted lines), at a given distance from the Sun. From the Green function solution (again sufficiently away from the boundaries of the propagation region) we can guess that, in the static limit, the peak of the product $p^2 \cdot \Phi_e$ scales like d^{-3} . This is indeed what we find in the plot, where the quantity $d^3 p^2 \Phi_e$ has been normalized to 1 in arbitrary units for $d = 10$ pc; the figure shows also the departure from such scaling in case of a non-stationary source, with the result for approaching, static and departing sources essentially coinciding only in the limit of small distances and large energies. For moderate to large distances the height of the peaks increases (decreases) for a source which has passed by (is approaching). The spectral shapes are also very different, with the sharp cutoffs at low energy enforced by the mismatch between the time interval from positron emission to detection and the energy loss timescale, which increases at lower energies. Positron propagation is treated according to model "AH" as introduced above; such model has $h_h = 4$ kpc and hence

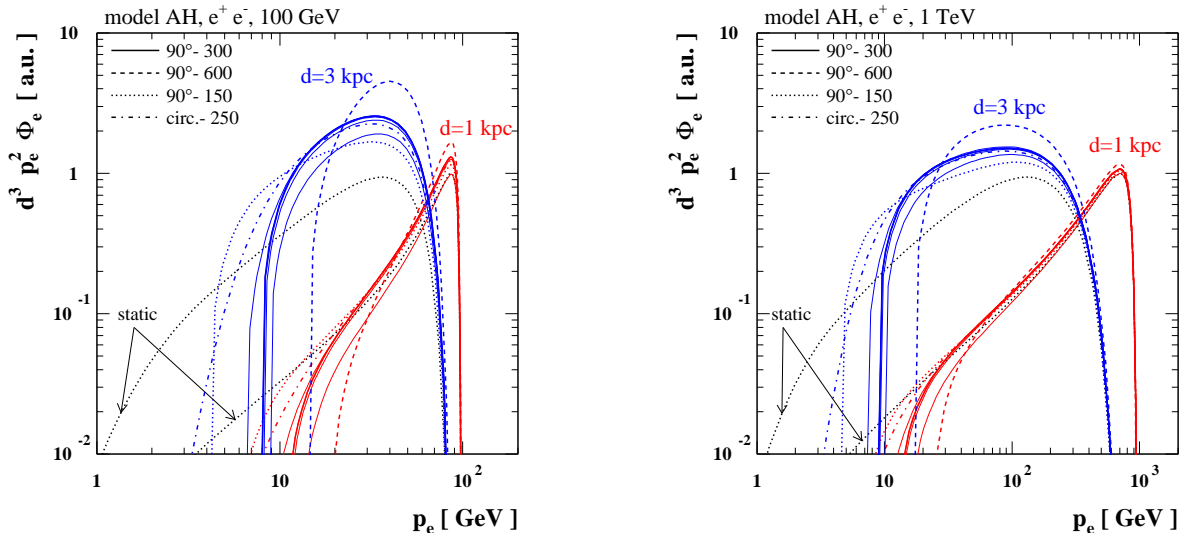


FIG. 3: Local positron flux spectral shape for a point source made of 100 GeV (left panel) or 1 TeV (right panel) WIMPs annihilating into monochromatic $e^+ e^-$, in the benchmark propagation model AH. The two values of d refer to the distances which the source has from the observer at the time the flux is measured and after the source has passed in the vicinity of the observer; the set of curves displayed refer to a few sample orbits for the source (see the text for details).

an approaching source at $d = 3$ kpc, along the vertical trajectory we are considering, has just entered the diffusion region and induces a local positron flux which is marginal compared to the flux from the same source after passing by and being on the other side of the trajectory at the same distance. Even after the source has left the diffusion region there is still a population of positrons which has been left behind contributing to the local flux, especially at low energies: here a larger d just reflects a longer time interval since the injection time and hence a more efficient degrading of the injected high energy positrons to small energies. In the right panel of Fig. 2, we take one of the cases plotted in the left panel, namely a source moving away from the observer and being at $d = 1$ kpc at the time of observation, and show instead the dependence of the spectral shape and the normalization of the measured flux on the benchmark models chosen for propagation and energy losses. Indeed the differences between the various cases are rather striking; this gives a feeling for the fact that there are large uncertainties related to propagation in our problem, which are not resolved tuning the model, as we did, to local measurements of secondary to primary nuclei ratios. Furthermore, there are potentially other relevant issues which we do not address in our simplified approach. E.g., we expect some dependence of the results on how boundary conditions are treated in the diffusion model: we are adopting here the standard approach of a spatially constant diffusion coefficient and free escape (i.e. the diffusion coefficient going to infinity) as a sharp transition at the vertical boundaries; this is the same approach followed, e.g., in Galprop. Considering a less sharp transition between the two regimes, with, e.g., an exponential vertical scaling of the diffusion coefficient as proposed by [26], we would obtain smoother cutoffs in the spectra of sources at large distances shown in the left panel of Fig. 2. A gradient in the energy loss term would also mildly affect the prediction for the local positron flux.

Fig. 3 considers the cases for a lighter and heavier WIMP (respectively, 100 GeV and 1 TeV) and, referring again to the propagation model AH, discusses the dependence of the locally measured positron flux on the orbit of the source, having chosen two sample values of the present distance of the source from the observer (1 kpc and 3 kpc and source moving away from the observer). The thick solid lines correspond to the source moving along a vertical orbit intersecting the Galactic plane at 10 pc from the observer (i.e., the same orbit as in Fig. 2), while thin solid lines are obtained in a few cases in which this scale is varied up to 1 kpc for $d = 1$ kpc, and to 2 kpc for $d = 3$ kpc, or inclining the orbit from vertical to a 45° incident angle; as it can be seen, such cases are essentially equivalent and show that what is actually relevant for the result is how much time the source spend within a distance from the observer corresponding to diffusion length λ (with λ depending on the emission and observation energies). Such time is about the same for all solid lines, while it changes if the source speed is changed. The dashed and dotted lines refer to the same orbit as for the thick solid line but with a source speed which is, respectively, twice as large and half of it, namely 600 km s^{-1} and 150 km s^{-1} versus 300 km s^{-1} . The dash-dotted lines refer instead to a circular orbit with velocity matching the observed circular velocity, i.e. about 250 km s^{-1} . For comparison spectral shapes in the static

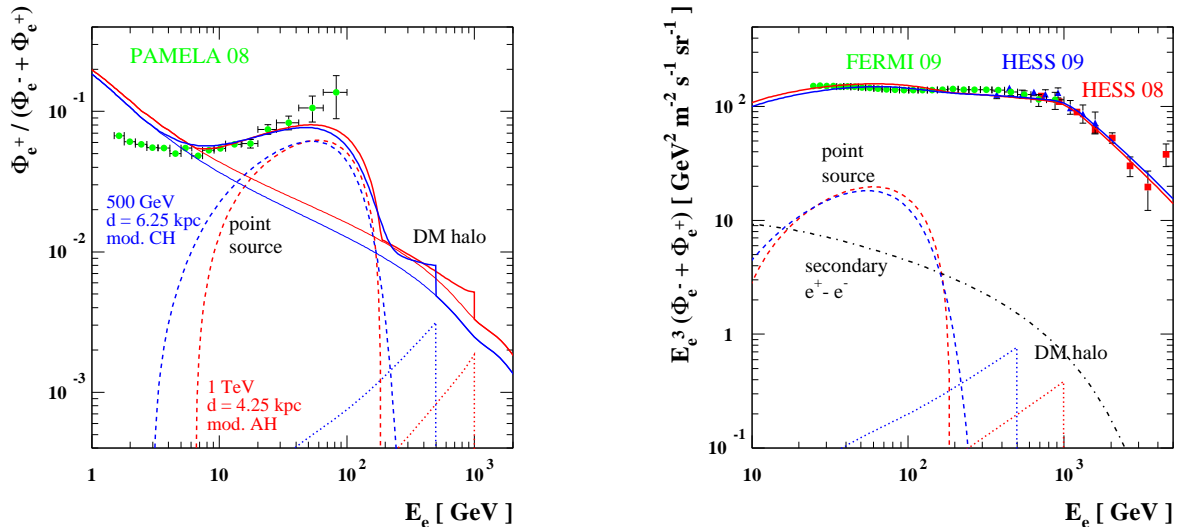


FIG. 4: Two examples of fits of the PAMELA positron fraction (left panel) and of the sum of the electron and positron fluxes (right panel) with a component due to DM annihilations in a substructure. The monochromatic e^+e^- final state of annihilation has been considered, as well as two sample values of the DM mass. The fit was performed assuming that the primary electron spectral index and normalization follows from the FERMI data.

limit are also displayed. The picture emphasizes further the fact that the encounter with a dark matter point-source determines a transient in the local positron flux, and that the static approximation is roughly valid only for nearby sources, for which the energy of the measured positrons is not significantly different from the energy at emission, or for very energetic positrons.

We have focussed the discussion on DM sources with a monochromatic positron spectrum, still it can be very simply extended to DM sources with a generic positron emission spectrum (which can be obviously thought as a superposition of line spectra for different masses and annihilation rates), along the same patterns regarding the dependence on distance and energy.

IV. A NON-STATIC POINT SOURCE VERSUS PAMELA AND FERMI ELECTRON/POSITRON DATA

As an application of the general discussion outlined in the previous Section, and to introduce a focus on a specific case despite the many ingredients and parameters involved in the problem, we consider the possibility of a major contribution from a single non-static DM point-source to the local electron/positron spectrum as recently measured by PAMELA [1] and FERMI [2].

For what concerns the background from ordinary astrophysical electrons and positrons, we will consider two possibilities. In the first scenario, the bulk of the "all-electron" spectrum measured by FERMI is due to primary electrons emitted in supernova cosmic-ray sources (with only a mild contamination, at the 10-20% level, from secondary electrons and positrons), and, hence, we can use this data-set to derive the electron spectral index at the sources. The second possibility is that the FERMI measurement has actually found an extra electron and, possibly, positron source, comparable to standard contributions at about 100 GeV or so, and dominating at high energy up to the cutoff found by HESS at about 1 TeV [35]; in this second scenario, we assume that the primary electron spectrum is softer and can be inferred from preliminary (less accurate) lower energy data on the electron-only spectrum presented by PAMELA [36], while the extra contribution is dominated by a single DM source.

Starting with the first background choice, we show in Fig. 4 (left panel) two examples of fits of the PAMELA positron fraction at high energy with a component due to DM annihilations in a subhalo. The fits have been obtained with sample values of the WIMP mass and a given annihilation channel, respectively 500 GeV and 1 TeV and the monochromatic e^+e^- final state. We have also assumed that the source moves with constant velocity $v_s = 300 \text{ km s}^{-1}$ on the trajectory perpendicular to the Galactic plane already introduced for Fig. 2. Looping over the propagation models discussed in the previous Sections, we have extracted the best-fit values for the source distance and the total annihilation rate in the source Γ . For a given propagation model, the background is inferred normalizing the proton

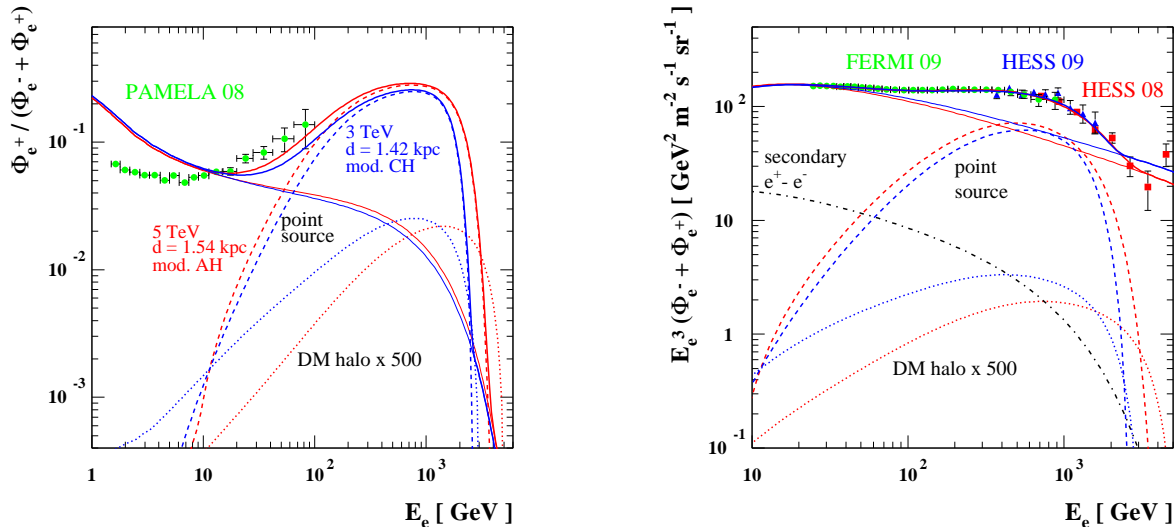


FIG. 5: Two further examples of fits of the PAMELA positron fraction (left panel) and of the sum of the electron and positron fluxes (right panel) with a component due to DM annihilations in subhalo. With respect to Fig. 4, we are now considering a different annihilation channel, i.e. $\tau^+ \tau^-$, and that the primary electron spectral index is slightly harder than the one you would infer from the FERMI data.

flux to the locally observed spectrum, making a prediction for the secondary electron and positron components using the Galprop package, and deriving the primary electron spectral index and normalization from the FERMI data. Including then the DM component, the fit to the PAMELA, FERMI and HESS data (the HESS datasets are rescaled within systematic uncertainties to match the normalization from FERMI) is performed allowing for a 20% variation in the normalization of the secondary spectra (reflecting various uncertainties on their modelling) and on the primary electrons, as well as a slight tilt in the primary electron spectral index; the fit disregards PAMELA datapoints below 10 GeV, since the force-field method we are implementing to take into account solar modulation, with modulation parameter of 0.55 GV, is probably not sufficiently accurate, and a modulation which takes into account the charge sign should be implemented instead [1]. For a given WIMP mass, and for all propagation parameters except for the thin halo model (model B), this procedure produces configurations with moderate to small χ^2 . They are restricted in a rather narrow range of allowed distances; however this range shifts with WIMP mass, choice of the propagation model and the velocity of the source along the orbit. The parameters for the two sample models obtained from the fit and plotted in Fig. 4 are given in the first two rows of Table I.

Analogously, Fig. 5 shows two sample fits of the data in the case of a primary electron spectral index slightly softer, according to the picture mentioned at the beginning of this Section. Since we need to account for a positron/electron exotic contribution up to 1-2 TeV, DM WIMPs needs to be rather heavy (e.g., we take 5 TeV and 3 TeV), while the choice of the annihilation channel is again not critical (we chose to refer to the case of pair annihilation into the $\tau^+ \tau^-$ final state). The results from the fit are reported in the last two rows of Table I. A few issues should be stressed looking at this table. First, for all the four selected models, the χ^2 indicate fairly good fits, although not exceptionally good (one should also take into account that, especially for FERMI, errors in the data-set are correlated,

	M_χ GeV	annihilation channel	Γ 10^{36} s^{-1}	\mathcal{V}_s kpc^3	prop. model	d kpc	$\Phi_\gamma(E > 0.1 \text{ GeV})$ $\text{cm}^{-2} \text{ s}^{-1}$	χ^2 (d.f.=50)
1	1000	e^+/e^-	20.9	$5.3 \cdot 10^5$	AH	4.25	$1.2 \cdot 10^{-8}$	46.7
2	500	e^+/e^-	73.4	$4.6 \cdot 10^5$	CH	6.25	$1.6 \cdot 10^{-8}$	42.3
3	5000	τ^+/τ^-	1.9	$12.6 \cdot 10^5$	AH	1.54	$1.1 \cdot 10^{-8}$	44.4
4	3000	τ^+/τ^-	2.4	$5.5 \cdot 10^5$	CH	1.43	$1.4 \cdot 10^{-8}$	60.9

TABLE I: Sample DM models

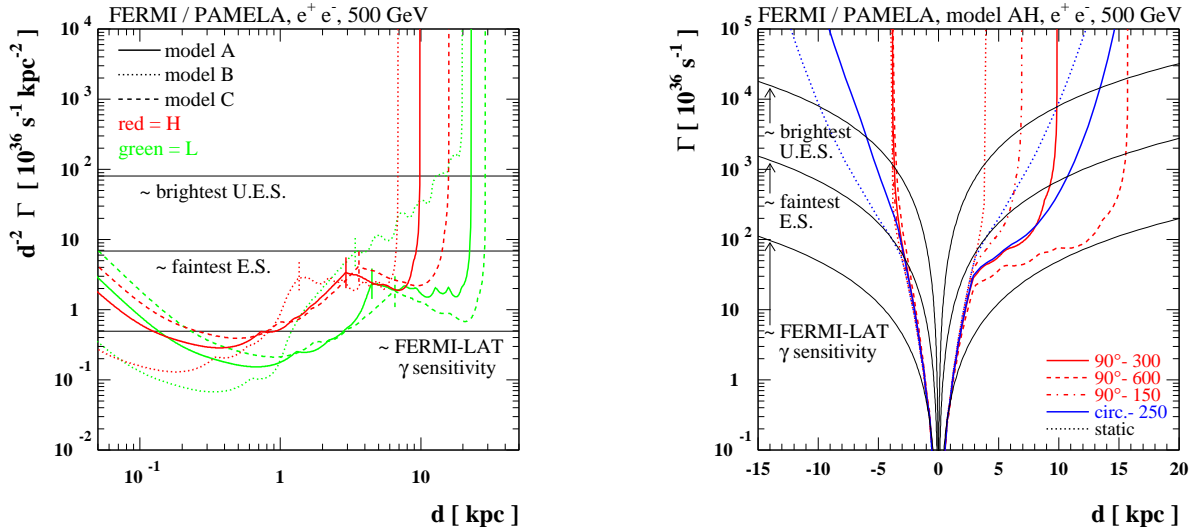


FIG. 6: Upper limits on the total annihilation rate Γ derived from the PAMELA data on the positron ratio and FERMI data on the all electron flux. A sample WIMP model is considered ($M_\chi = 500$ GeV and monochromatic e^+e^- final state), while we loop over propagation model configurations (left panel) and a few possibilities for the point source orbit (right panel). Results are compared to the level of Γ required to match either the brightest unidentified EGRET source, the faintest source detected by EGRET and the level of the γ -ray sensitivity for FERMI.

while we have simply added in quadrature statistical and systematic errors); our interest is, however, to show the feasibility of the framework, rather than playing with all possible uncertainties in the background and the signal to improve the fits further (and indeed a slight readjustment of the background could lead to better fits in all cases). A second issue is that the values which we find for the total annihilation rate Γ are very large for all models, as one sees converting them to the annihilation volume \mathcal{V}_s under the hypothesis that the annihilation cross section is of the order $\sigma v \simeq 3 \cdot 10^{-26} \text{ cm}^3 \text{ s}^{-1}$ (this is, roughly speaking, the level needed for a thermal relic WIMP to match the DM density in the Universe in case of standard assumptions for the Universe thermal history, and without invoking an enhancement in the cross section going from the freeze-out to the zero temperature limit, see, e.g., [9]). Annihilation volumes of the order of $10^5 - 10^6 \text{ kpc}^3$ are much larger than typical values predicted for DM substructures in N-body simulations of hierarchical clustering for Milky-Way size DM halos, with a realization probability for a configuration containing these sources, supposing one can extrapolate from the results shown in Ref. [19] for static sources, below few in 10^{-4} . On the other hand, in a different scenarios, such as the one in which the adiabatic formation of an intermediate mass black hole drives a sharp enhancement of the dark matter density inside the hosting substructure [37], the probability density of \mathcal{V}_s for these sources has a peak at about 10^6 kpc^3 and a tail extending to much larger values [15]. There is also the possibility that the reference value $\sigma v \simeq 3 \cdot 10^{-26} \text{ cm}^3 \text{ s}^{-1}$ is a significant underestimate of the pair annihilation cross section, and in this case \mathcal{V}_s would be appropriately downscaled.

Having shown that it is not manifestly implausible to interpret current positron/electron data within the single DM substructure scenario, the examples chosen for Figs. 4 and 5 question the standard methods applied to extract model-independent informations on the DM candidate: It is usually assumed that interpreting an excess as a DM signal gives an estimate of the DM particle mass when the energy threshold for the excess is detected, that the spectral shape of the excess determines the dominant annihilation channel, while the normalization is mainly an indicator of the level of the pair annihilation rate. Here, instead, the threshold is just setting a lower limit to the DM particle mass, since the energy at which the exotic component dies out depends also on the distance of the DM point-source. Regarding the shape of the spectrum, we have shown that this is a transient, keeping little memory of the spectrum at the source, and indeed, in the plot, the spectral shapes of the single source contribution and that from the smooth DM halo component are sensibly different in all examples. Finally, the level of the induced flux depends mainly on the product $\sigma v \cdot \mathcal{V}_s$, and it is difficult to give any solid estimate for the annihilation volume \mathcal{V}_s .

In Table I, we quote the prediction for the gamma-ray flux, integrated above 100 MeV, induced by the DM point-source in the four selected models: in the first two cases, with only monochromatic e^+/e^- as tree-level final state of annihilation, the flux is due to photons emitted as a final state radiation (FSR), with the rate and photon energy distribution for the $\chi\chi \rightarrow e^+e^-\gamma$ which are estimated in terms of the lowest order process $\chi\chi \rightarrow e^+e^-$ and in the approximation for $m_e \ll M_\chi$ (see, e.g., [38] and references therein; an eventual model-dependent "internal

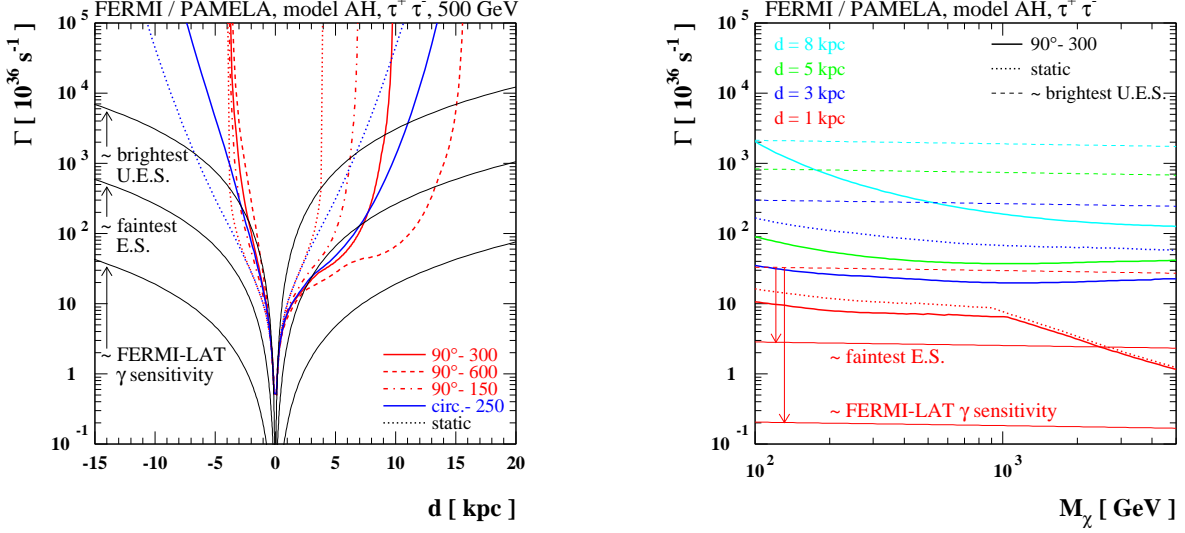


FIG. 7: Upper limits on the total annihilation rate Γ derived from the PAMELA data on the positron ratio and FERMI data on the all electron flux. The left panel is specular to the right panel of Fig. 7, but for the $\tau^+ \tau^-$ final state. In the right panel the mass scale for the DM candidate is varied and a few sample values of the distance for a source moving away from the observed along a vertical orbit are considered. Results are compared to the level of the Γ required to match either the brightest unidentified EGRET source, the faintest source detected by EGRET and the level of the γ -ray sensitivity for FERMI.

bremsstrahlung” contribution [39] is not included here). For the last two cases, the annihilation into τ^+/τ^- gives rise to decay chains containing neutral pions, which in turn decay to two photons; this process is accounted for by linking to the Pythia Montecarlo simulations as provided by the DarkSUSY package [40]. The level of the integrated gamma-ray fluxes, slightly above $1 \cdot 10^{-8} \text{ cm}^{-2} \text{ s}^{-1}$, is much lower than the one for the brightest unidentified EGRET source, i.e. about $7 \cdot 10^{-7} \text{ cm}^{-2} \text{ s}^{-1}$, or the level of the faintest source detected by EGRET, i.e. about $6 \cdot 10^{-8} \text{ cm}^{-2} \text{ s}^{-1}$ [41] (in a more detailed comparison one should consider also the fact that the energy spectra for the sources proposed here are sensibly softer than typical spectra for EGRET sources), but well within the sensitivity for the FERMI LAT instrument, about $4 \cdot 10^{-9} \text{ cm}^{-2} \text{ s}^{-1}$ considering intermediate to high latitudes and a 2 year data taking period [42] (again we are not taking into account spectral features, and also the fact that the sensitivity we quote for a DM signal was computed based on a gamma-ray background as extrapolated from EGRET GeV measurements of the diffuse gamma-ray emission which are not being confirmed by FERMI and will have to be sensibly lowered, see, e.g., [43]). This is a trend we see in general.

In Fig. 6, we compute the upper limit to the total annihilation rate Γ from the PAMELA data on the positron ratio and from the FERMI data on the “all-electron” flux (limits are extracted separately for the two datasets, allowing for extra freedom in the background normalization and spectral index; the most stringent one is displayed). These constraints are compared to the values of Γ corresponding to an integrated γ -ray luminosity at the level of the brightest unidentified EGRET source, of the faintest source detected by EGRET and of the FERMI γ -ray sensitivity. We have chosen a benchmark WIMP model, with $M_\chi = 500 \text{ GeV}$ and annihilating into monochromatic $e^+ e^-$. We display the results for: *i*) the reference vertical orbit and different propagation models (left panel, the displayed cases are the same as in Fig. 2, see the relative discussion in the text; the values of d refer to the distance of the point source from the observer at the time when the positron flux is measured, after the source has passed in the neighborhood of the observer); *ii*) the reference propagation model AH and a few possibilities for the point-source orbit (right panel, the sample orbits are a subset of those considered in Fig. 3; negative d refers to an approaching source, positive d to a source moving away from the observer). In the right panel of Fig. 6, we also sketch the error that can be induced by estimating positron constraints assuming the stationary limit. Dotted curves refer to static point-sources and show (making the comparisons with the appropriate color coding) that the bounds, except for nearby sources, are systematically overestimated for approaching sources and greatly underestimated for sources moving away from the observer. Clearly, the gamma-ray luminosity of a point-source scales with $1/d^2$. The scaling with distance, or better with time, of the local positron flux depends on many different ingredients which are hard to extract from observations. The picture, however, is intuitively clear: unless the DM point-source is extremely close to the observer inducing a very large gamma-ray flux (at a level which can be already excluded by EGRET), it can generate a substantial contribution to the electron/positron flux measured by PAMELA and FERMI, without being

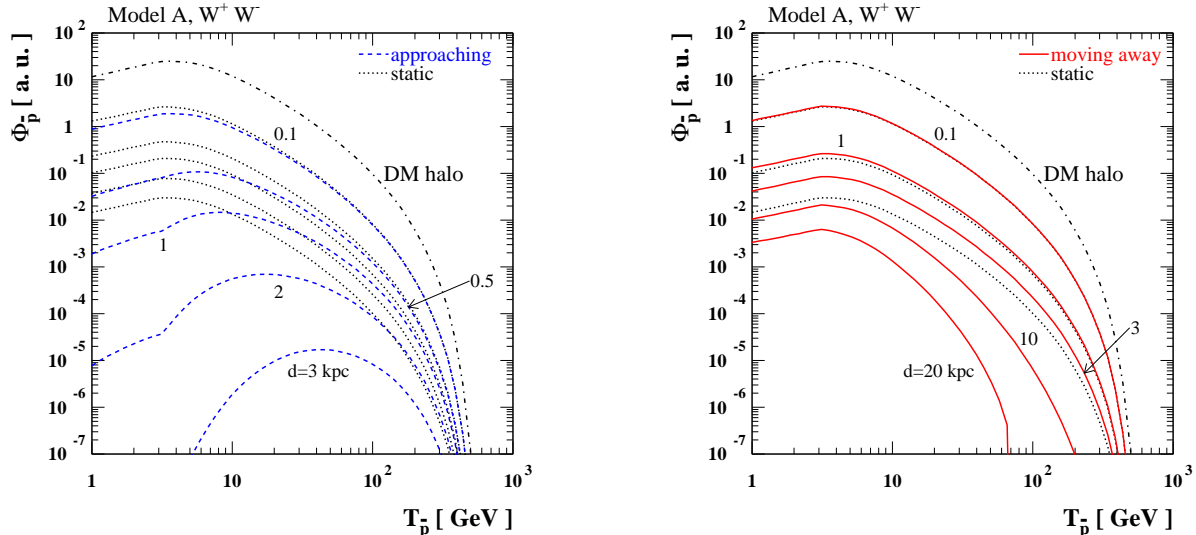


FIG. 8: Spectral shapes for the local antiproton flux due to a dark matter point source moving on a vertical orbit with constant velocity $v_s = 300 \text{ km s}^{-1}$ and for different values of the distance d of the source at the time of observation. In the left panel, the source is getting closer to the observer. In the right panel, the source, after passing in the vicinity of the observer, is moving away. A WIMP mass of 500 GeV and pair annihilations into $W^+ W^-$ have been assumed, as well as the propagation model A. For comparison, spectral shapes for a static source at the corresponding distances and for pair annihilations in the smooth DM halo are also shown.

in conflict with present gamma-ray observations. In particular, we expect, for intermediate distances, the balance to lean towards the electron/positron side since there is a time interval during which electrons/positrons go through a diffusion transient while the gamma-ray intensity decreases as the inverse of time squared. When the diffusion transient is over and the local positron population becomes negligible, i.e. at large positive distances in the plot, the gamma-ray limit takes over again. On the other hand, if a substantial contribution to the positron flux measured by PAMELA is actually due to a DM point source, it is unlikely that such source will not be detected by FERMI in γ -rays. This does not necessarily mean that it will be identified as a DM source. Indeed, FERMI will measure spectra only up to about 300 GeV and spectral features might not be easily identifiable, as well as the cross correlation with the positron flux is not anymore unambiguous, as we already stressed.

These conclusions do not depend critically on the WIMP model, as we show in Fig. 7. In the left panel, we consider the same configurations of the right panel in Fig. 6, but now for a WIMP model annihilating into $\tau^+ \tau^-$. In this case, the γ -ray yield is enhanced (being the π^0 -decay channel open) and the electron/positron yield is softer; still, at intermediate distances, a picture inducing a sizable local flux of positrons is not in conflict with the EGRET observations, but again within the FERMI γ -ray sensitivity. In the right panel of Fig. 7, we show the constraints on Γ obtained considering a few values for the source distance (still moving away from the observer on a vertical orbit with a velocity of 300 km s^{-1}) and varying the WIMP mass. The interplay between electron/positron and gamma-ray observations is changing only slightly with mass, while it is again evident that the static approximation may be misleading.

V. ANTIPROTONS FROM A DARK MATTER POINT SOURCE

We focus now the discussion on the possibility that dark matter pair annihilations within a substructure give rise to an antiproton yield. This is possible if the final states of annihilation include weak gauge bosons or quarks, instead of leptons only, as we considered so far. Analogously to the positron case, in the limit of a point-like dark matter substructure, the antiproton source function takes the form:

$$Q_{\bar{p}}(\vec{r}, t, E) = \delta^3[\vec{r} - \vec{r}_p(t)] \frac{dN_{\bar{p}}}{dE} \Gamma, \quad (8)$$

where $dN_{\bar{p}}/dE$ is the differential antiproton yield per annihilation and Γ is the total dark matter annihilation rate in the source already introduced above. Solving the propagation equation with this source function, we find the

corresponding number density per unit energy:

$$n(\vec{r}, E, t) = \frac{dN_{\bar{p}}}{dE} \Gamma \int_{-\infty}^t dt_0 G(\vec{r}, t, E; \vec{r}_p, t_0), \quad (9)$$

where the Green function G is given in Appendix B. As for positron, it is instructive to consider its approximate form by neglecting boundary conditions; assuming at first that also antiprotons annihilations in the gas disc along propagation play a minor role, G goes like:

$$G \simeq \frac{1}{\pi^{3/2} [\lambda_p(E, t, t_0)]^3} \exp \left[-\frac{|\vec{r} - \vec{r}_p(t_0)|^2}{[\lambda_p(E, t, t_0)]^2} \right], \quad (10)$$

where the diffusion length depends explicitly on time: $\lambda_p(E, t, t_0) = 2\sqrt{(t-t_0)D(E)}$. Suppose for simplicity that the substructure is moving along a straight line trajectory with constant velocity \vec{v}_s , namely $\vec{r}_p(t_0) = \vec{r}_t + \vec{v}_s(t_0 - t)$; in this case G can be rewritten in the form:

$$G \simeq \frac{1}{8\pi^{3/2} D^{3/2} (t-t_0)^{3/2}} \exp \left[-\left(\frac{t_s}{t-t_0} - 2\sqrt{\frac{t_s}{t_d}} c_\theta + \frac{t-t_0}{t_d} \right) \right] \quad (11)$$

where we have introduced a "static" timescale $t_s \equiv d_t^2/4D$, with $d_t = |\vec{r}_t - \vec{r}|$ being the distance between the point-source and the observer at the time of observation (which would be, of course, the distance between the point-source and the observer at all times in the static limit), and a "dynamical" timescale $t_d \equiv 4D/|\vec{v}_s|^2$, and we have defined c_θ as the cosine of the angle between the vectors \vec{v}_s and $\vec{r}_t - \vec{r}$ (which is negative for a source approaching the observer and positive for those moving away). We recognize that t_d and t_s are the appropriate quantities to compare for a first guess on whether proper motion is relevant or not in estimating antiproton fluxes from point sources; in particular, Eq. (11) can be integrated over time, giving:

$$\int_{-\infty}^t dt_0 G \simeq \frac{1}{4\pi D |\vec{r} - \vec{r}_t|} \exp \left[-\frac{2t_s}{t_d} + 2\sqrt{\frac{t_s}{t_d}} c_\theta \right]. \quad (12)$$

In the limit for $t_d \gg t_s$, this expression correctly reduces to the Green function of the three dimensional Laplacian, while for $t_d \sim 2t_s$ we see that proper motion starts to become important. For typical values of the propagation parameters in the model, we find:

$$\frac{t_d}{2t_s} = \frac{8D^2(E)}{d_t^2 v_s^2} \simeq 1.5 \frac{D_1^2 E_{10}^{2\delta} 10^{2\delta-1.2}}{d_{t,1}^2 v_{300}^2}, \quad (13)$$

where E_{10} is antiproton energy in units of 10 GeV and $d_{t,1}$ is the source distance in units of 1 kpc. As for the positrons, we find the effect of proper motion to be negligible either in the limit of nearby sources or going to high energies, while we expect it to be significant in the other cases.

Actually, Eq. (10) and (11) contain an oversimplification, since they were derived neglecting antiprotons annihilations during propagation, an effect which defines a third timescale that could also be relevant: depending on energy, the antiproton loss via annihilation can be much larger than the leakage from the boundaries of the diffusion region. When including this extra timescale, the expression for G becomes less transparent; we show instead results for a few sample cases obtained by implementing the exact Green function. In Fig. 8, we plot the spectral shape for the local antiproton flux from a source moving along the reference trajectory, namely a path perpendicular to the Galactic plane and intersecting it at a short distance from the observer, with the source moving at constant velocity $v_s = 300 \text{ km s}^{-1}$. We have also chosen the propagation model A, and defined the dark matter model through a sample value for the WIMP mass, $M_\chi = 500 \text{ GeV}$, and assuming that the annihilation is dominantly into $W^+ W^-$ pairs. As in the previous plots, d refers to the distance of the source from the observer at the time of observation and is used instead of a time variable to compare more easily to the static limit (dotted curves in the plot). There is a evident transient at small and intermediate energies, soon after the source has entered the diffusion region; the spectrum starts to fully match the static limit case only when the source arrives very close to the observer. Moving away from the observer, the scaling with distance is less severe than in the static limit and a contribution to the local antiproton flux persists much later than the time at which the source has left the propagation region (the vertical boundary is at $h_h = 4 \text{ kpc}$ in model A). Since high energy antiprotons diffuse more efficiently, at late times the spectral shape becomes steeper and starts again to differ sensibly from the shape of the component due to pair annihilations in the smooth dark matter halo (dash-dotted line in the plot). Note that the latter, contrary to the positron case, traces rather closely the shape of static point-sources.

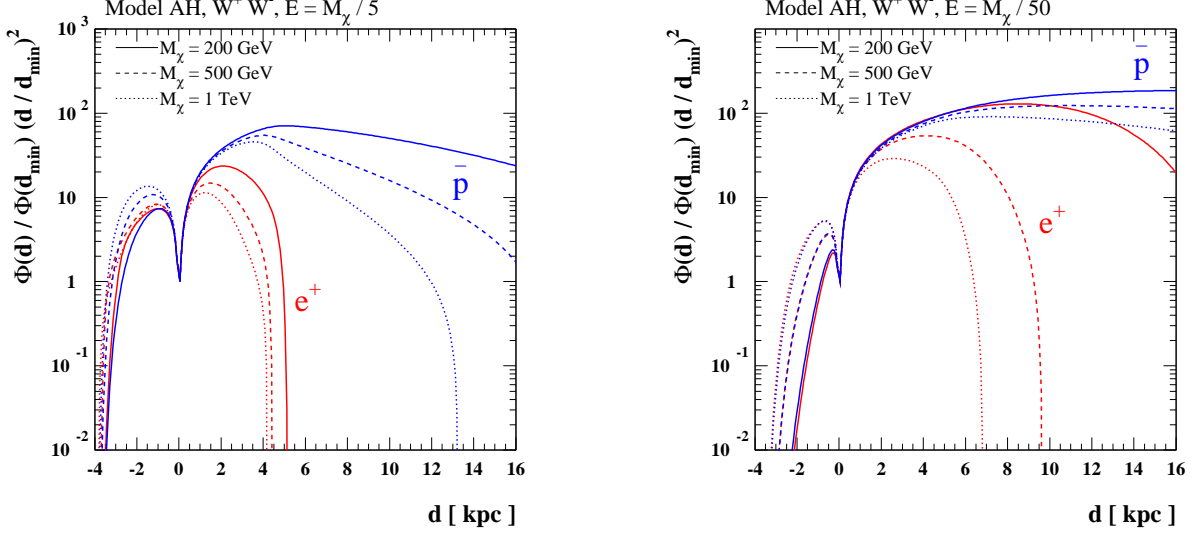


FIG. 9: The locally measured antiproton and positron fluxes as a function of the distance of the point source (negative distances label an approaching source, positive values a source moving away) normalized to the fluxes at a closest encounter distance $d_{min} = 50$ pc and to the scaling with distance of the companion induced gamma-ray flux, i.e. $1/d^2$. W^+W^- annihilation channel is considered (giving rise at the same time to antiprotons, positrons and photons) and three sample values of the WIMP mass M_χ . The antiproton and positron fluxes are plotted at the energies E which are equal to $M_\chi/5$ (left panel) and $M_\chi/50$ (right panel).

The W^+W^- annihilation channel is a copious source of positrons and gamma-rays (mainly from the production and decay of pions). In Fig. 9, we compare the scaling with distance (i.e. time) of the locally measured antiproton and positron fluxes at an energy corresponding to a fraction of the WIMP mass ($1/5$ and $1/50$, respectively, in the left and right panels) for three sample values of M_χ . Both antimatter fluxes are normalized to the scaling with distance of the induced gamma-ray emission, which goes simply like $1/d^2$. The ratio between charged-particle fluxes to the gamma-ray flux increases rapidly around $d = 0$ since the local number density of positrons and antiprotons decreases less severely when the distance from the source is smaller than the corresponding diffusion length. At negative d , i.e. for a source approaching the observer, one can see again the transients due to the fact that the source has just entered the diffusion region; these transients are essentially specular in the two cases. On the other hand, the contribution to the local antiproton population tends to survive much longer than for the positron component. When the source is moving away, the antiproton flux scales, at least at intermediate distances and except for very energetic antiprotons, like $1/d^2$; positrons have instead much sharper transients, due to the efficient energy loss term.

Fig. 9 has been obtained for the reference propagation model (AH, with the "H" labeling the energy loss configuration for positrons only) and the reference trajectory. As for the positrons, we expect the results for the antiproton flux to depend on the choice of the propagation parameters and the orbit for the point source. This is illustrated in Fig. 10: in the left panel, we show the scaling of the locally measured antiproton flux with distance considering two sample WIMP masses, two sample energies and the benchmark trajectory, while looping over the three reference propagation models. The main effect here is due to the increase in the diffusion coefficient going from model B to model A and then to model C, as well as to the boundary conditions, entering more critically for the thin-halo model B ($h_h = 1$ kpc); note, however, that even for model B a sizable contribution to the local flux may be due to sources which are well outside the diffusion region and that would not be included in the static limit treatment. In the right panel of Fig. 10, we consider instead a few of the orbits that we have already introduced to discuss positron fluxes, with the pattern for source velocities which is analogous here; note that in the circular orbit case the transient following a close encounter can be sufficiently long lasting for the induced antiproton population to persist up to the next close encounter (what we plot is the "equilibrium" configuration after a couple of full orbits).

Finally, in Fig. 11, we summarize the picture by comparing, for a WIMP model with W^+W^- annihilation channel, the constraints on the total annihilation rate which are set by the latest measurements by PAMELA of the antiproton to proton ratio [44], the electron/positron measurements by PAMELA and FERMI, as well as searches for point γ -ray sources by EGRET. Projected limits for the FERMI γ -ray telescope are also shown. Analogously to the case of the smooth DM halo component, we find for a DM substructure contribution that if WIMP annihilates in a channel in which antiprotons are copiously emitted, the measured antiproton flux sets tighter constraints than

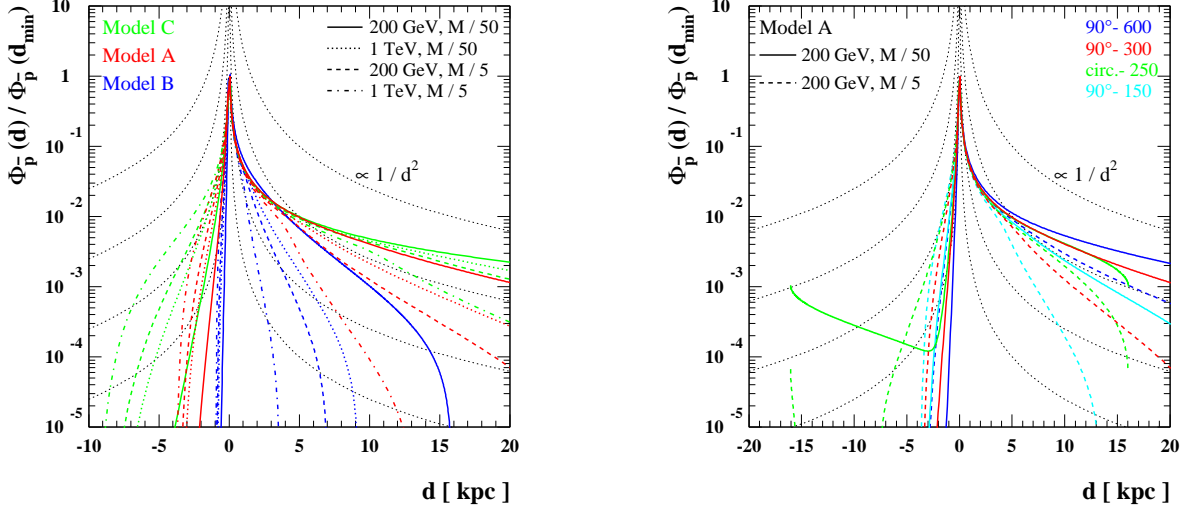


FIG. 10: Scaling of the locally measured antiproton flux with the distance of the point source from the observer (negative distances label an approaching source, positive values a source moving away), for two WIMP masses M_χ (200 GeV and 1 TeV) and two sample energies E (equal to $M_\chi/5$ and $M_\chi/50$), and assuming pair annihilations into W^+W^- . In the left panel, the results refer to the standard vertical trajectory and to our three benchmark propagation models A, B & C (intermediate, thin-halo & thick-halo, see text for details). In the right panel, for the propagation model A, the color coding refers to different orbits, namely three vertical trajectories with velocities of the source changing from 300 to 600 or 150 km s^{-1} , and a circular orbit in the Galactic plane with velocity matching the local circular velocity 250 km s^{-1} .

electron/positron data, except possibly for extremely heavy DM candidates. This trend is reinforced going to larger distances. The information from EGRET is inconclusive, while FERMI is going to cover most, if not all, the parameter space currently probed by antiproton or positron searches. The displayed results refer to a source moving along the reference vertical trajectory, approaching or moving away from the observer; however, analogous conclusions hold for other configurations. The extension to other WIMP annihilation channels also leads to similar results.

VI. EXTRA FEATURES OF POSITRON/ELECTRON EMISSION FOR A DM POINT SOURCE

A. A gamma-ray component from inverse Compton emission on starlight

Radiative emissions are unavoidably associated to electron/positron yields; in particular, the Inverse Compton (IC) radiation component due to the interaction of high energy electrons on optical starlight is peaked in the range between tens to hundreds of GeV and may be sizable for the intense dark-matter lepton emitters we have been considering.

The IC photon emissivity is obtained by folding, at any given point within the diffusion region, the IC emission power with the electron/positron number density, see, e.g., [45]:

$$j_{IC}(\nu, \vec{r}, t) = 2 \int_{m_e}^{M_\chi} dE P_{IC}(\vec{r}, E, \nu) n(\vec{r}, E, t), \quad (14)$$

where the IC power is given by:

$$P_{IC}(\vec{r}, E, \nu) = ch\nu \int d\epsilon \frac{dn_\gamma}{d\epsilon}(\epsilon, \vec{r}) \sigma(\epsilon, \nu, E) \nu \quad (15)$$

where ϵ is the energy of the target photons, $dn_\gamma/d\epsilon$ is their differential energy spectrum and σ is the Klein–Nishina cross section. The spatial dependence and spectrum of the number density of starlight photons can be computed from photometric maps of the Galaxy; we will adopt the model implemented in the public release of the Galprop numerical package [25]. On the other hand, the analytic solution introduced in Section III for computing the electron/positron number density n was obtained assuming a spatially constant electron/positron energy loss term, and, hence, also

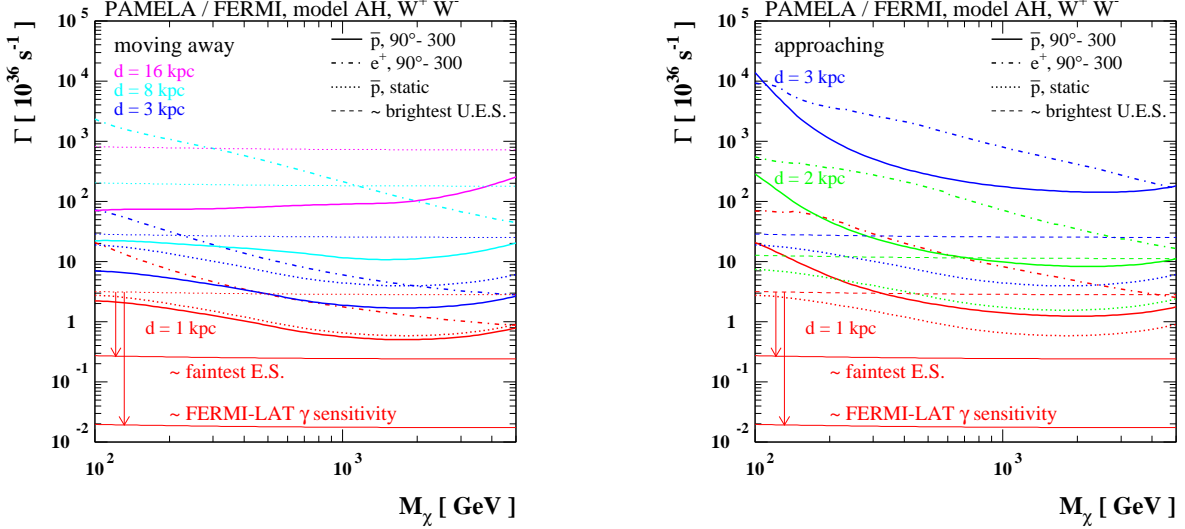


FIG. 11: Upper limits on the total annihilation rate Γ derived from the PAMELA data on the antiproton fraction (solid lines), PAMELA data on the positron ratio and FERMI data on the all electron flux (dash-dotted lines). The source is moving along the reference vertical trajectory and is approaching the observer (left panel) or moving away from the observer (right panel). Results are compared to the level of the Γ required to match either the brightest unidentified EGRET source, the faintest source detected by EGRET and the level of the γ -ray sensitivity for FERMI.

a mean value for the background starlight density, rather than its value as a function of the spatial coordinates. This should not be regarded as a severe inconsistency, since the IC on starlight is just one of the effects contributing to the energy loss term, which main uncertainty is related to synchrotron emission on background magnetic fields. Having computed the IC emissivity field as in Eq. 14, the relative γ -ray flux for a local observer is obtained simply by summing contributions along the line of sight.

An example is given in Fig. 12, where we refer again to the model introduced at the beginning of the discussion, namely a point source composed by 500 GeV WIMPs annihilating into monochromatic electrons and positrons and moving on a vertical orbit intersecting the Galactic plane at a short distance from the observer, see Figs. 2 and 6. The propagation scenario considered is the AH model (recall that in this model the vertical scale height of the diffusion region is 4 kpc) and the time variable is again replaced by the distance from the observer. Having assumed a velocity of the point source of 300 km s^{-1} , we consider three sample cases, i.e. $d = 1, 3, 5 \text{ kpc}$ with the source that has passed close to the observer and is now moving away. The induced IC flux (solid lines) is shown for three different directions of observation, all at the longitude $l = 180^\circ$ (i.e. opposite to the Galactic center), with latitude $b = 90^\circ$ (the direction towards the point source in our example), $b = 75^\circ$ or $b = 60^\circ$. We plot also the background level corresponding to the emission from Galactic cosmic-rays (dotted lines) computed with Galprop, and the DM-induced γ -ray component due to FSR at the source (which is obviously present only in the direction of the DM substructure). The normalization of the total annihilation rate, or of the annihilation volume, has been chosen by saturating the current limits from PAMELA or FERMI, see the results in Fig. 6. This explains the relative strength of the FSR components. One can see that the IC flux in the direction of the source can be as large as the FSR contribution (for $d = 1 \text{ kpc}$) or even larger (for $d = 3 \text{ kpc}$). Most notably, the spatial size of the IC emission is significant, inducing a signal larger than the background even tens of degrees away from the source. Consider, however, that the case displayed here is the most favorable, since the source is located in the portion of the sky with the faintest Galactic background, and we have not included the uncertain extragalactic component. For $d = 5 \text{ kpc}$, i.e. for the source outside the diffusion region, the IC term drops dramatically. This is due to the fact that there is no fresh source of high energy electrons and positrons, and the ones injected along the transit of the source through the diffusion region have rather rapidly degraded their energy. Therefore, there is no efficient high energy source to up-scatter starlight photons to γ -ray frequency. The trend is probably exaggerated by the fact that we are assuming a sharp boundary for the propagation region, while a smoother boundary condition would be certainly more physical and would probably lead to a smoother transition between the cases, $d = 3 \text{ kpc}$ to the $d = 5 \text{ kpc}$.

From the sample case discussed, we can infer that it is rather likely that if the local positron flux receives a sizable contribution from a single point-source, the induced IC flux is a relevant target for the FERMI γ -ray telescope. A more thorough discussion about this point is delayed to an upcoming dedicated analysis.

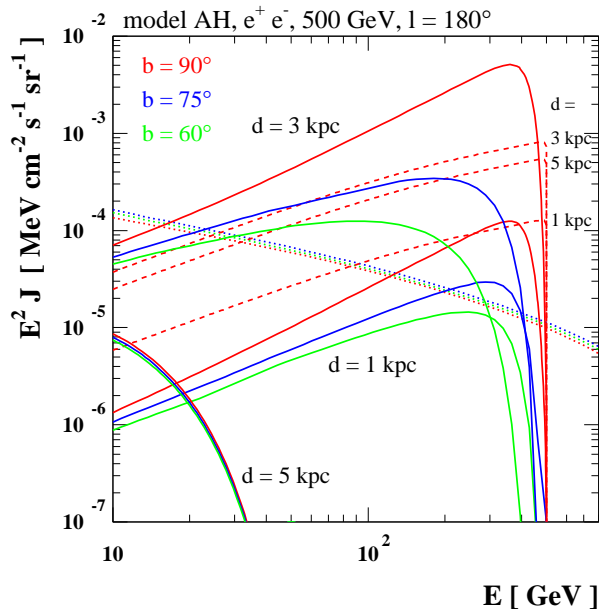


FIG. 12: γ -ray spectra for a DM point-source composed by 500 GeV WIMPs annihilating into monochromatic electrons and positrons, and moving along the reference vertical trajectory. The solid lines refer to the IC emissivity and are computed for three different directions of observation labeled by the latitude b (the longitude is $l = 180^\circ$); dashed lines refer to the FSR component in the direction of the source, while dotted lines show the Galactic γ -ray background. The DM signals are computed for three sample distances of the source, assuming that, for each distance, the normalization of the total annihilation rate in the source is the maximum allowed by current PAMELA and FERMI electron/positron data, see the limits derived in Fig. 6.

B. Dipole anisotropy in the electron/positron spectrum

As pointed out by recent analyses (see e.g., [46, 47, 48, 49]), a single nearby point-like source (e.g., a pulsar), being the dominant local positron source at high energy, induce an anisotropy which could be at a detectable level. In this Section, we reconsider this possibility in the context of DM substructure. We take into account proper motion effects, which are not relevant for bursting-like sources as pulsars. We assume the dominant contribution to the anisotropy to be given by the dipole term. In order to detect an anisotropy along a certain direction at a good confidence level, the required number of events has to be very large. Therefore, although the anisotropy in the positron spectrum would be higher than in the total electron plus positron spectrum, we refer to the latter, being the detection prospects for FERMI much more promising than for PAMELA.

If the anisotropy is dominated by the dipole term, the intensity at a given point as a function of the direction of observation has only one maximum. The degree of dipole anisotropy can be defined by the quantity $\delta = (I_{max} - I_{min}) / (I_{max} + I_{min})$, where I_{max} and I_{min} are the maximum and minimum $e^+ + e^-$ intensity with respect to direction. Expanding the intensity in spherical harmonics up to the dipole term, we have: $I(\theta, \phi) \simeq \bar{I} + \delta \bar{I} \cos \theta + \sin \theta (I_1^{-1} e^{-I\phi} + I_1^1 e^{I\phi})$, where θ is the angle with respect to the direction of maximal anisotropy, $\bar{I} = (I_{max} + I_{min}) / 2 = (I(\theta = 0) - I(\theta = \pi)) / 2$, and I_1^{-1} and I_1^1 are angle-independent coefficients. Note that contrary to the case of a stationary point-source (with homogeneous and isotropic propagation parameters), the ϕ -dependent terms of the dipole are not null.

Although the direction of maximal anisotropy (chosen, e.g., as the z -axis) is, in general, unknown, we can define the particle flux F along such direction by integrating over all the possible directions the projection over z of the intensity, i.e., $F \simeq \int d\Omega I \cos \theta \simeq 4/3 \pi \delta \bar{I}$, and by estimating it as $F \simeq D |\nabla n|$. The latter is obtained in the diffusion approximation [50], but it is valid at first order (i.e., for small anisotropies) also when including energy losses. Moreover, we assume the anisotropies in directions orthogonal to z to be subdominant (i.e., $\partial_z n \simeq \nabla n$). By equating the two expressions for F , one gets [51]:

$$\delta = \frac{3D}{c} \frac{|\nabla n_{tot}|}{n_{tot}} = \frac{3D}{c} \frac{|\nabla n_{DM}|}{(n_{DM} + n_{CR})}, \quad (16)$$

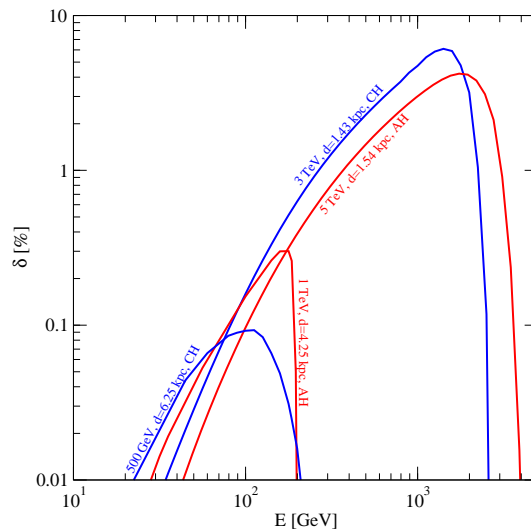


FIG. 13: Dipole anisotropy of the electron plus positron spectrum as a function of the energy for the four sample DM scenarios in Table I.

where n_{DM} denotes the contribution to the $e^+ + e^-$ number density induced by a DM substructure, n_{CR} is the contribution from cosmic-rays, and $n_{tot} = n_{DM} + n_{CR}$.

Neglecting boundary conditions, $|\nabla n_{DM}|$ is given by the gradient of Eq. 5:

$$|\nabla n_{DM}(\vec{r}, p, t)| = \left[\sum_{i=1}^3 \left(\Gamma \int_{t_i}^t dt_0 \left| \frac{\dot{p}(p_0)}{\dot{p}(p)} \right| \frac{dN_{e^+}}{dp_0} 2 \frac{x_i - x_{i,p}(t_0)}{\lambda(p, p_0)^2} G(\vec{r}, p; \vec{r}_p(t_0), p_0) \right)^2 \right]^{1/2}, \quad (17)$$

with p_0 obtained from $\Delta\tau = t - t_0$ and $x_i = x, y, z$ for $i = 1, 2, 3$, respectively.

We plot in Fig. 13, the degree of dipole anisotropy for the benchmark DM scenarios in Table I. Comparing models 3 and 4, describing sources at analogous distance and with analogous local spectrum, one can note that, as intuitive, an approaching source would induce a higher anisotropy than a moving-away source (both on a straight-line trajectory). On the other hand, for sources at moderate distance the mismatch is quite small and the picture is similar to the stationary case. The degree of anisotropy is strongly and inversely correlated to the diffusion length (see Eq. 17). Although the benchmark DM models 1 and 2 induce a very similar local spectrum (see Fig. 4) and describe substructures moving away from us on a vertical trajectory at the same velocity, in the second case the electrons and positrons undergo a greater diffusion before reaching us, and the anisotropy is suppressed with respect to the first case. Note that the maximum of the curves in Fig. 13 occur at larger energy than the peaks in Figs. 4 and 5, being the diffusion and the related wash-out of anisotropies less effective at high energy. The degree of dipole anisotropy for the benchmark models in Fig. 13 can be observable by FERMI in few years of data taking. On the other hand, the predictions for the anisotropy associated to a DM substructure suffer of many theoretical uncertainties, as in the case of the spectrum, and, depending on the trajectory, the degree of anisotropy can be suppressed or slightly enhanced with respect to an analogous (i.e., at analogous distance from the observer) stationary point-like case.

VII. CONCLUSIONS

We have discussed the contribution to the local antimatter fluxes due to individual WIMP DM substructures, accounting for the substructure proper motion. We have derived analytic solutions to the propagation equation as appropriate for a time-dependent positron and antiproton primary sources, identifying the relevant quantities to discriminate whether proper motion effects are relevant or not. We found that, for both positrons and antiprotons, the static limit is a fair approximation only in the case of high energy particles and nearby sources, while it fails in all other situations. The discussion has involved a few benchmark DM candidates and a few sample orbits for the substructure.

As an application of the general discussion, we focused first on WIMPs annihilating into leptons only, and we derived sample fits of the PAMELA positron excess and FERMI all-electron data. The fits have been obtained starting from some arbitrary values of the WIMP mass, demonstrating that, for a single non-static DM point-source, it is no longer

true that one can extract from the data, in a unique way, as extensively done in recent analyses, model independent particle physics observables, such as the DM mass, the annihilation yield and the pair annihilation cross section. Indeed, the threshold of the local electron/positron spectrum cannot be used as a sure indicator of the DM particle mass, being possibly set by the distance of the DM substructure. The relation between the shapes of the injection spectrum and of the propagated spectrum is not straightforward for a non-static DM substructure, which behaves as a transient source. Moreover, the annihilation rate depends on the product of the pair annihilation cross section times the unknown annihilation volume of the substructure, rather than on σv only.

The PAMELA positron excess can be explained in such a scenario, provided that a large annihilation rate in the substructure is considered. This requires either a large annihilation volume (much larger than typical values predicted for DM substructures in N-body simulations, but viable for scenarios accounting for the adiabatic formation of an intermediate mass black hole in the substructure) and/or a pair annihilation cross section significantly enhanced with respect to the reference thermal value.

We have then used PAMELA and FERMI electron/positron data to derive, under different configurations, limits to the total annihilation rate in the DM source. These limits have been compared to the bounds extracted from the γ -ray luminosities associated to the same DM models. The general trend is that the γ -ray signal induced by a DM point-source, giving a sizable contribution to the local positron flux, is below the level of the brightest unidentified EGRET sources, but well above the FERMI γ -ray telescope sensitivity.

We have also discussed WIMP models giving raise to an antiproton yield through pair annihilations in the substructure, as in the case with W^+W^- as final state of annihilation. Analogously to the electron/positron case, single DM sources inducing a significant contribution to the local antiproton flux can be detected by FERMI in γ -rays (on the other hand, as for the smooth DM halo component, a positron/electron flux at the level of PAMELA and FERMI data can be hardly obtained in such WIMP models without violating antiproton limits).

Finally, we sketched two further features in connection to positron/electron emission from a DM point-source, namely the spectral and angular shape of γ -ray flux induced by inverse Compton emission on starlight, and the dipole anisotropy in the electron/positron spectrum. We have shown that, potentially, both of them could be used to test the scenario proposed here.

Acknowledgements

We would like to thank P. D. Serpico for useful discussions. M.R. acknowledges funding by, and the facilities of, the Centre for High Performance Computing, Cape Town. P.U. is partially supported by the European Community's Human Potential Programme under contracts MRTN-CT-2006-035863.

-
- [1] O. Adriani *et al.* [PAMELA Collaboration], arXiv:0810.4995 [astro-ph].
 - [2] A. A. Abdo *et al.* [The Fermi LAT Collaboration], arXiv:0905.0025 [astro-ph.HE].
 - [3] J. Chang *et al.*, Nature **456** (2008) 362.
 - [4] S. Torii *et al.* [PPB-BETS Collaboration], arXiv:0809.0760 [astro-ph].
 - [5] S. Rudaz and F. W. Stecker, Astrophys. J. **325** (1988) 16.
 - [6] J. R. Ellis, R. A. Flores, K. Freese, S. Ritz, D. Seckel and J. Silk, Phys. Lett. B **214** (1988) 403.
 - [7] M. Kamionkowski and M. S. Turner, Phys. Rev. D **43** (1991) 1774.
 - [8] G. Jungman, M. Kamionkowski and K. Griest, Phys. Rept. **267** (1996) 195 [arXiv:hep-ph/9506380].
 - [9] L. Bergstrom, Rept. Prog. Phys. **63** (2000) 793 [arXiv:hep-ph/0002126].
 - [10] G. Bertone, D. Hooper and J. Silk, Phys. Rept. **405** (2005) 279 [arXiv:hep-ph/0404175].
 - [11] L. Bergstrom, J. Edsjo and G. Zaharijas, arXiv:0905.0333 [astro-ph.HE].
 - [12] P. Meade, M. Papucci, A. Strumia and T. Volansky, arXiv:0905.0480 [hep-ph].
 - [13] N. Arkani-Hamed, D. P. Finkbeiner, T. R. Slatyer and N. Weiner, Phys. Rev. D **79** (2009) 015014 [arXiv:0810.0713 [hep-ph]].
 - [14] Y. Nomura and J. Thaler, arXiv:0810.5397 [hep-ph].
 - [15] P. Brun, G. Bertone, J. Lavalle, P. Salati and R. Taillet, Phys. Rev. D **76** (2007) 083506 [arXiv:0704.2543 [astro-ph]].
 - [16] J. Lavalle, Q. Yuan, D. Maurin and X. J. Bi, Astron. & Astrophys. **479** (2008) 427 arXiv:0709.3634 [astro-ph].
 - [17] D. Hooper, A. Stebbins and K. M. Zurek, arXiv:0812.3202 [hep-ph].
 - [18] T. Bringmann, J. Lavalle and P. Salati, arXiv:0902.3665 [astro-ph.CO].
 - [19] P. Brun, T. Delahaye, J. Diemand, S. Profumo and P. Salati, arXiv:0904.0812 [astro-ph.HE].
 - [20] M. Kuhlen and D. Malyshev, arXiv:0904.3378 [hep-ph].
 - [21] J. Binney and S. Tremaine, "Galactic Dynamics", Princeton University Press, 2008, second edition.
 - [22] M. J. Reid *et al.*, arXiv:0902.3913 [astro-ph.GA].

- [23] T.K. Gaisser, “Cosmic rays and particle physics”, Cambridge University Press, 1991.
- [24] A. W. Strong, I. V. Moskalenko and V. S. Ptuskin, *Ann. Rev. Nucl. Part. Sci.* **57** (2007) 285 [arXiv:astro-ph/0701517].
- [25] A. W. Strong and I. V. Moskalenko, *Astrophys. J.* **509** (1998) 212 [arXiv:astro-ph/9807150].
- [26] C. Evoli, D. Gaggero, D. Grasso and L. Maccione, *JCAP* **0810**, 018 (2008) [arXiv:0807.4730 [astro-ph]].
- [27] W. R. Webber, M. A. Lee and M. Gupta, *Astrophys. J.* **390** (1992) 763.
- [28] D. Maurin, F. Donato, R. Taillet and P. Salati, *Astrophys. J.* **555** (2001) 585 [arXiv:astro-ph/0101231].
- [29] I. V. Moskalenko, A. W. Strong, J. F. Ormes and M. S. Potgieter, *Astrophys. J.* **565** (2002) 280 [arXiv:astro-ph/0106567].
- [30] A. D. Panov *et al.*, arXiv:0707.4415 [astro-ph].
- [31] H. S. Ahn *et al.*, *Astropart. Phys.* **30** (2008) 133 [arXiv:0808.1718 [astro-ph]].
- [32] Engelmann, J. J., Ferrando, P., Soutoul, A., Goret, P., and Juliusson, E. *Astron. Astrophys.* **233** (1990) 96
- [33] Swordy, S. P., Mueller, D., Meyer, P., L’Heureux, J., and Grunsfeld, J. M. *Astrophys. J.* **349** (1990) 625
- [34] T. A. Porter, I. V. Moskalenko, A. W. Strong, E. Orlando and L. Bouchet, *Astrophys. J.* **682** (2008) 400 [arXiv:0804.1774 [astro-ph]].
- [35] F. Aharonian *et al.* [H.E.S.S. Collaboration], *Phys. Rev. Lett.* **101** (2008) 261104 [arXiv:0811.3894 [astro-ph]].
- [36] Talk by O. Adriani available at <http://www.crlab.rise.waseda.ac.jp>.
- [37] G. Bertone, A. R. Zentner and J. Silk, *Phys. Rev. D* **72** (2005) 103517 [arXiv:astro-ph/0509565].
- [38] L. Bergstrom, G. Bertone, T. Bringmann, J. Edsjo and M. Taoso, arXiv:0812.3895 [astro-ph].
- [39] L. Bergstrom, T. Bringmann and J. Edsjo, *Phys. Rev. D* **78** (2008) 103520 [arXiv:0808.3725 [astro-ph]].
- [40] P. Gondolo, J. Edsjo, P. Ullio, L. Bergstrom, M. Schelke and E. A. Baltz, *JCAP* **0407** (2004) 008 [arXiv:astro-ph/0406204].
- [41] V. Pavlidou, J. M. Siegal-Gaskins, B. D. Fields, A. V. Olinto and C. Brown, *Astrophys. J.* **667** (2008) 27 [arXiv:0710.0619 [astro-ph]].
- [42] E. A. Baltz *et al.*, *JCAP* **0807** (2008) 013 [arXiv:0806.2911 [astro-ph]].
- [43] Talks at ENTApP DARK MATTER workshop 2009 by I. V. Moskalenko and A. W. Strong. Transparencies at <http://indico.cern.ch/conferenceDisplay.py?confId=44160>
- [44] O. Adriani *et al.*, *Phys. Rev. Lett.* **102** (2009) 051101 [arXiv:0810.4994 [astro-ph]].
- [45] G. Rybicki and A.P. Lightman, 1979, ‘Radiative Processes in Astrophysics’, John Wiley & Sons Inc.
- [46] I. Buesching, O. C. de Jager, M. S. Potgieter and C. Venter, arXiv:0804.0220 [astro-ph].
- [47] D. Hooper, P. Blasi and P. D. Serpico, *JCAP* **0901** (2009) 025 [arXiv:0810.1527 [astro-ph]].
- [48] D. Grasso *et al.* [FERMI-LAT Collaboration], arXiv:0905.0636 [astro-ph.HE].
- [49] I. Cernuda, arXiv:0905.1653 [astro-ph.HE].
- [50] Berezhinskii, V. S., Bulanov, S. V., Dogiel, V. A., and Ptuskin, V. S., 1990, Amsterdam: North-Holland, 1990, edited by Ginzburg, V.L.,
- [51] V. L. Ginzburg and S. I. Syrovatskii, *The Origin of Cosmic Rays*, New York: Macmillan, 1964.
- [52] E. A. Baltz and L. Wai, *Phys. Rev. D* **70** (2004) 023512 [arXiv:astro-ph/0403528].
- [53] E. A. Baltz and J. Edsjo, *Phys. Rev. D* **59**, 023511 (1998) [arXiv:astro-ph/9808243].
- [54] S. Thoudam, 2008, *MNRAS*, 388, 335 [arXiv:0804.4730 [astro-ph]].

APPENDIX A: SOLUTION TO THE PROPAGATION EQUATION FOR POSITRONS

We present here a solution to Eq. 1 which is valid for a generic non-stationary primary source of electrons and positrons in a disc-like galaxy and with the following simplifying assumptions: We consider a model with diffusion coefficient and energy loss term that are a function of momentum only, while they are assumed to be spatially constant within the cylindrical propagation volume; we impose free escape at the vertical boundary of the diffusion region (i.e. that the equilibrium number density vanishes at $z = \pm h_n$) and neglect the radial boundary (i.e. in the limit of radial size of the diffusion region R_h being much larger than h_h). Reacceleration and convection are also neglected. In Cartesian coordinates Eq. (1) becomes:

$$\frac{\partial n(\vec{r}, p, t)}{\partial t} = Q(\vec{r}, p, t) + D(p)\Delta n - \frac{\partial}{\partial p}(\dot{p}n) \quad (\text{A1})$$

The solution described here is a generalization of the one derived in Ref [52] to the case of diffusion coefficient D and momentum gain/loss term \dot{p} which are generic function of the particle momentum p ; the notation we use is hence analogous to that of [52]. We start by introducing $N \equiv -\dot{p}n$, and solve the equation for N rather than for n , using the Green function method and neglecting at first the vertical boundary condition:

$$-\frac{1}{\dot{p}}\frac{\partial G}{\partial t} + \frac{D}{\dot{p}}\Delta G - \frac{\partial G}{\partial p} = \delta(\vec{r} - \vec{r}_0)\delta(t - t_0)\delta(p - p_0). \quad (\text{A2})$$

Going to the Fourier transforms in the variables \vec{r} and t , we find:

$$\left[-\frac{1}{\dot{p}}(-i\omega + D|\vec{k}|^2) - \frac{\partial}{\partial p} \right] \bar{G} = e^{i\vec{k}\cdot\vec{r}_0 + i\omega t_0} \delta(p - p_0). \quad (\text{A3})$$

The solution of this equation is easily derived replacing the electron/positron momentum p with a double change of variables:

$$\tau = - \int_p^{p_{\max}} \frac{d\tilde{p}}{\dot{p}(\tilde{p})} \quad \text{and} \quad \lambda^2 = 4 \int_{\tau_0}^{\tau} d\tilde{\tau} D(\tilde{\tau}) = -4 \int_p^{p_0} d\tilde{p} \frac{D(\tilde{p})}{\dot{p}(\tilde{p})}, \quad (\text{A4})$$

and considering first the case $p \neq p_0$. The physically relevant solution vanishes for $p > p_0$ since we will not include energy gain effects, but only energy losses (i.e., the term $\dot{p}(p)$ in the equations above is negative); we find:

$$\bar{G} = \bar{G}_0 e^{[i\omega\Delta\tau - |\vec{k}|^2\lambda^2/4]}, \quad (\text{A5})$$

where we defined $\Delta\tau = \tau(p) - \tau(p_0)$ and the constant \bar{G}_0 is obtained integrating Eq. (A3) around $p = p_0$:

$$-\hat{G}\Big|_{p_0-}^{p_0+} = \bar{G}_0 = e^{i\vec{k}\cdot\vec{r}_0 + i\omega t_0}. \quad (\text{A6})$$

Taking now the inverse Fourier transform, we find the Green function:

$$G_{free}(\vec{r}, t, p; \vec{r}_0, t_0, p_0) = \frac{\exp\left[-\frac{|\vec{r}-\vec{r}_0|^2}{\lambda^2}\right]}{\pi^{3/2}\lambda^3} \delta((t-t_0) - \Delta\tau), \quad (\text{A7})$$

where it is now manifest to recognize λ as a diffusion length scale and $\Delta\tau$ as an energy loss timescale; the subscript "free" was added to the Green function since we have not included the vertical boundary condition yet. This is implemented with the image charge method, i.e. having defined $z_n \equiv (-1)^n z + 2nh_h$, and having factorized the Green function as $G_{zb} = G_{zb-ti} \cdot \delta((t-t_0) - \Delta\tau)$, G_{zb-ti} is given by:

$$G_{zb-ti}(\vec{r}, p; \vec{r}_0, p_0) = \frac{\exp\left[-\frac{(x-x_0)^2 + (y-y_0)^2}{\lambda^2}\right]}{\pi^{3/2}\lambda^3} \sum_{n=-\infty}^{+\infty} (-1)^n \exp\left[-\frac{(z_n - z_0)^2}{\lambda^2}\right]; \quad (\text{A8})$$

it is easy to verify that $G_{zb}(x, y, z = \pm h_h, t; \vec{r}_0, t_0) = 0$. The density per unit energy is then:

$$n(\vec{r}, p, t) = -\frac{1}{\dot{p}} \int_{-\infty}^{+\infty} dx_0 \int_{-\infty}^{+\infty} dy_0 \int_{-h_h}^{+h_h} dz_0 \int_{-\infty}^t dt_0 \int_p^{p_{max}} dp_0 G_{zb}(\vec{r}, t, p; \vec{r}_0, t_0, p_0) Q(\vec{r}_0, t_0, p_0). \quad (\text{A9})$$

In case the source Q is point-like, such as the point-like dark matter substructure in Eq. (3), entering the diffusion region at the time t_i , the density per unit energy becomes the expression in Eq. (5), or equivalently takes the form (which is the one we use for numerical calculations):

$$n(\vec{r}, p, t) = \Gamma \int_{t_i}^t dt_0 \left| \frac{\dot{p}(p_0)}{\dot{p}(p)} \right| \frac{dN_{e^+}}{dp_0} G_{zb-ti}(\vec{r}, p; \vec{r}_p(t_0), p_0), \quad (\text{A10})$$

where p_0 is obtained from the numerical inversion of the relation $\tau(p) - \tau(p_0) = t - t_0$. Finally, we just remark that in case of a stationary diffuse electron/positron source, $n(\vec{r}, p)$ reduces to the familiar expression derived in the literature [53] (again generalized to D and \dot{p} which are arbitrary functions of p):

$$n(\vec{r}, p) = -\frac{1}{\dot{p}(p)} \int_{-\infty}^{+\infty} dx_0 \int_{-\infty}^{+\infty} dy_0 \int_{-h_h}^{+h_h} dz_0 \int_p^{p_{max}} dp_0 G_{zb-ti}(\vec{r}, p; \vec{r}_0, p_0) Q(\vec{r}_0, p_0), \quad (\text{A11})$$

i.e. for a stationary axisymmetric source (i.e. for $Q(\vec{r}_0, p_0) = Q(R_0, z_0, p_0)$ with R_0 the radial variable in a cylindrically symmetric system):

$$n(\vec{r}, p) = \int_p^{p_{max}} \frac{dp_0}{|\dot{p}(p)|} \int_0^{R_h} dR_0 \tilde{I}_0\left(\frac{2RR_0}{\lambda^2}\right) \frac{2R_0 \exp\left[-\frac{(R-R_0)^2}{\lambda^2}\right]}{\sqrt{\pi}\lambda^3} \int_{-h_h}^{+h_h} dz_0 \sum_{n=-\infty}^{+\infty} \exp\left[-\frac{(z_n - z_0)^2}{\lambda^2}\right] Q(R_0, z_0, p_0), \quad (\text{A12})$$

where we introduced the function $\tilde{I}_0(x) = \exp(-x) I_0(x)$, with $I_0(x)$ the modified Bessel function of first kind.

APPENDIX B: SOLUTION TO THE PROPAGATION EQUATION FOR ANTIPROTONS

Analogously to the positron case, we sketch here a solution to Eq. 1 which can be applied to a generic non-stationary primary source of antiprotons. We assume again that the propagation region is a cylinder and that the diffusion coefficient is spatially constant within it; we impose free escape as vertical boundary condition, while neglecting the boundaries in the radial direction. We still do not include reacceleration and convection, as well as energy losses give a negligible effect for antiprotons. We include instead the antiproton absorption effect, assuming it is mainly due to a thin gas disk, with gas target density constant in space and localized at $z = 0$. In Cartesian coordinates Eq. (1) becomes:

$$\frac{\partial n(\vec{r}, E, t)}{\partial t} = Q(\vec{r}, E, t) + D(E)\Delta n - P(E)\delta(z)n \quad (\text{B1})$$

with the term accounting for \bar{p} losses due to collisions with the interstellar medium being $P(E) = 2h_g n_H v(E)\sigma_p(E)$, where h_g is half of the gas disc height, and the gas disk is assumed to be made of hydrogen with constant density n_H . The solution sketched here is analogous to the one presented in Ref. [54] in a different context. It is derived through the Green function method, neglecting at first the vertical boundary condition:

$$D(E) \left(\frac{\partial^2 G}{\partial x^2} + \frac{\partial^2 G}{\partial y^2} + \frac{\partial^2 G}{\partial z^2} \right) - P(E)\delta(z)G - \frac{\partial G}{\partial t} = -\delta(\vec{r} - \vec{r}_0)\delta(t - t_0) \quad (\text{B2})$$

The following steps are to take the Fourier transforms in the x and y directions, i.e. $\bar{G} = \int_{-\infty}^{+\infty} dx \int_{-\infty}^{+\infty} dy G e^{ik_x x + ik_y y}$:

$$D(E) \frac{\partial^2 \bar{G}}{\partial z^2} - D(E)K^2 \bar{G} - P(E)\delta(z)\bar{G} - \frac{\partial \bar{G}}{\partial t} = -e^{ik_x x_0 + ik_y y_0} \delta(z - z_0) \delta(t - t_0) \quad (\text{B3})$$

with $K^2 = k_x^2 + k_y^2$, and to make a Laplace transformation in the t variable, i.e. $\hat{G} = \int_0^\infty dt \bar{G} e^{-st}$:

$$D \frac{\partial^2 \hat{G}}{\partial z^2} - (DK^2 + s)\hat{G} - P(E)\delta(z)\hat{G} = -e^{ik_x x_0 + ik_y y_0 - st_0} \delta(z - z_0) \quad (\text{B4})$$

Away from $z = 0$ and $z = z_0$, the equation takes the form:

$$\frac{\partial^2 \hat{G}}{\partial z^2} - \omega^2 \hat{G} = 0 \quad (\text{B5})$$

with $\omega = \sqrt{K^2 + s/D}$; the three solutions in the three distinct regions (i.e. the region between 0 and z_0 , and those below and above it, setting the appropriate boundary conditions at $z = \pm\infty$) are matched to find \hat{G} imposing its continuity and that (as one derives integrating Eq. (B4) around $z = z_0$ and $z = 0$):

$$D \frac{\partial \hat{G}}{\partial z} \Big|_{z_0^-}^{z_0^+} + e^{ik_x x_0 + ik_y y_0 - st_0} = 0 \quad \text{and} \quad D \frac{\partial \hat{G}}{\partial z} \Big|_{0^-}^{0^+} - P(E)\hat{G}(z=0) = 0. \quad (\text{B6})$$

One finds $\hat{G} = \hat{g} \cdot e^{ik_x x_0 + ik_y y_0 - st_0} / D$, where

$$\begin{aligned} \hat{g} &= \frac{\exp[-\omega(|z| + |z_0|)] |sign(z) - sign(z_0)|}{P/D + 2\omega} \frac{1}{2} \\ &+ \left\{ \frac{\exp[-\omega||z| - |z_0||]}{2\omega} - \frac{P/D \exp[-\omega(|z| + |z_0|)]}{2\omega(P/D + 2\omega)} \right\} \frac{|sign(z) + sign(z_0)|}{2}. \end{aligned} \quad (\text{B7})$$

This expression can be inverted analytically to recover G . One can take first the inverse Laplace transform and find:

$$\bar{G} = e^{ik_x x_0 + ik_y y_0 - (k_x^2 + k_y^2)\lambda_p^2/4} g(z, t; z_0, t_0) \quad (\text{B8})$$

with:

$$g(z, t; z_0, t_0) \equiv \frac{1}{\sqrt{\pi}\lambda_p} \exp\left[-\frac{(z - z_0)^2}{\lambda_p^2}\right] - \frac{1}{L} \exp\left[2\frac{|z| + |z_0|}{L} + \frac{\lambda_p^2}{L^2}\right] \operatorname{erfc}\left(\frac{\lambda_p}{L} + \frac{|z| + |z_0|}{\lambda_p}\right), \quad (\text{B9})$$

where we defined: $\lambda_p(E, t, t_0) = 2\sqrt{(t - t_0)D(E)}$ and $L(E) = 4D(E)/P(E)$. Finally, taking the inverse Fourier transform we find the Green function:

$$G_{free}(\vec{r}, t; \vec{r}_0, t_0) = \frac{1}{\pi\lambda_p^2} \exp\left[-\frac{(x-x_0)^2 + (y-y_0)^2}{\lambda_p^2}\right] g(z, t; z_0, t_0) \quad (\text{B10})$$

where the subscript "free" was added since we did not include the vertical boundary condition yet. As for the positron case, this is implemented with the image charge method, i.e. having defined $z_n \equiv (-1)^n z + 2nh_h$, the Green function is:

$$G_{zb}(\vec{r}, t; \vec{r}_0, t_0) = \frac{1}{\pi\lambda_p^2} \exp\left[-\frac{(x-x_0)^2 + (y-y_0)^2}{\lambda_p^2}\right] \sum_{n=-\infty}^{+\infty} (-1)^n g(z_n, t; z_0, t_0). \quad (\text{B11})$$

Note that the expression we found is analogous to Eq. A8 for positrons; actually switching off antiproton annihilations (i.e. setting $P(E) = 0$) the two expressions are formally identical, except that the definition of diffusion length here is different from the diffusion length introduced for positrons, with time appearing explicitly in λ_p for antiprotons rather than implicitly through the momentum loss as in the λ for positrons. The density per unit energy is then:

$$n(\vec{r}, E, t) = \int_{-\infty}^{+\infty} dx_0 \int_{-\infty}^{+\infty} dy_0 \int_{-h_h}^{+h_h} dz_0 \int_{-\infty}^t dt_0 G_{zb}(\vec{r}, t, E; \vec{r}_0, t_0) Q(\vec{r}_0, t_0, E). \quad (\text{B12})$$